

Temperature and bath size in exact diagonalization dynamical mean field theory

Ansgar Liebsch¹ and Hiroshi Ishida²

¹*Peter Grünberg Institute and Institute of Advanced Simulation,
Forschungszentrum Jülich, 52425 Jülich, Germany*

²*College of Humanities and Sciences, Nihon University, Tokyo 156, Japan*

(Dated: October 29, 2018)

Dynamical mean field theory (DMFT) combined with finite-temperature exact diagonalization is one of the methods to describe electronic properties of strongly correlated materials. Because of the rapid growth of the Hilbert space, the size of the finite bath used to represent the infinite lattice is severely limited. In view of the increasing interest in the effect of multi-orbital and multi-site Coulomb correlations in transition metal oxides, high- T_c cuprates, iron-based pnictides, organic crystals, etc., it is appropriate to explore the range of temperatures and bath sizes in which exact diagonalization provides accurate results for various system properties. On the one hand, the bath must be large enough to achieve a sufficiently dense level spacing, so that useful spectral information can be derived, especially close to the Fermi-level. On the other hand, for an adequate projection of the lattice Green's function onto a finite bath, the choice of the temperature is crucial. The role of these two key ingredients in exact diagonalization DMFT is discussed for a wide variety of systems in order to establish the domain of applicability of this approach. Three criteria are used to illustrate the accuracy of the results: (i) the convergence of the self-energy with bath size, (ii) quality of the discretization of the bath Green's function, and (iii) comparisons with complementary results obtained via continuous-time quantum Monte Carlo DMFT. The materials comprise a variety of three-orbital and five-orbital systems, as well as single-band Hubbard models for two-dimensional triangular, square and honeycomb lattices, where non-local Coulomb correlations are important. The main conclusion from these examples is that a larger number of correlated orbitals or sites requires a smaller number of bath levels. Down to temperatures of 5 to 10 meV (for typical band widths $W \approx 2$ eV) two bath levels per correlated impurity orbital or site are usually adequate.

PACS. 71.27+a Strongly correlated electron systems

Contents

1. Introduction
 2. ED DMFT Formalism
 - 2.1. Multi-Band Correlations
 - 2.2. Multi-Site Correlations
 - 2.3. Size of Hilbert Space
 - 2.4. Bath Discretization
 3. Results and Discussion
 - 3.1. Degenerate Three-Band Model
 - 3.2. Three-Band Materials
 - 3.3. Degenerate Five-Band Model
 - 3.4. Triangular Lattice
 - 3.5. Square Lattice
 - 3.6. Honeycomb Lattice
 4. Summary and Outlook
- Acknowledgments
- Appendix: Bath Discretization
- A.1. Degenerate Three-Band Model
 - A.2. Square Lattice
- References

1. INTRODUCTION

The study of strong Coulomb correlations is one of the central topics in condensed matter physics. A wide vari-

ety of phenomena, such as high- T_c superconductivity in the cuprates, paramagnetic metal insulator transitions, strong effective mass enhancements, and bad-metallic behavior are intimately related to electronic correlations not included in ordinary band theory. During the past two decades, dynamical mean field theory [1–8] (DMFT) has proved to be a highly useful scheme for the description of these kinds of phenomena in many materials. The virtue of DMFT is that intricate single-electron properties, associated with complex lattice geometries and unit cells, and many-electron interactions in partially filled, nearly localized atomic orbitals are treated on the same footing. Since the balance between kinetic energy and Coulomb repulsion depends in subtle ways on important parameters, such as temperature, pressure, and chemical doping, a sufficiently detailed treatment of all key ingredients is essential. The conceptual advance of DMFT is that the problem of the correlated infinite lattice is mapped onto the problem of a correlated impurity immersed in a bath whose self-energy is determined via a self-consistent iterative procedure. The effective impurity may consist of a single atom or a small cluster of atoms. Coulomb interactions within this impurity are treated numerically exactly. Thus, dynamical fluctuations, which give rise to spectral weight transfer between low and high energies, are fully taken into account. Spatial fluctuations, on the other hand, are either neglected,

as in local or single-site DMFT, or included only at short distances, as in cluster extensions of DMFT [9–12].

The main computational task in DMFT lies in the solution of the quantum impurity problem for which techniques such as numerical renormalization group [13, 14] (NRG), quantum Monte Carlo [15] (QMC), exact diagonalization [16] (ED), and other more approximate schemes can be used. For multi-band materials and clusters involving several atoms, the most accurate and versatile approaches are QMC and ED. The focus in the present work is on ED at finite temperatures [17–21]. The key idea in ED is to discretize the continuum of the infinite lattice via a finite set of bath levels and to solve the many-body problem involving correlated impurity and finite bath exactly. Originally applied to the one-band Hubbard model [16], it soon was realized that this approach is limited to a small number of bath levels because of the exponentially growing Hilbert space. The usefulness of ED DMFT for strongly correlated materials involving several orbitals or sites was therefore far from evident.

The purpose of this work is to demonstrate that finite-temperature ED DMFT is in fact a highly useful and accurate many-body scheme that is applicable to systems including (so far) up to five correlated orbitals and clusters up to six correlated sites. Typically, this implies two to three bath levels per orbital or site. In certain cases, only one bath level per orbital or site was found to give satisfactory results. This conclusion seems surprising in view of the fact that, to obtain well converged results for the single-band Hubbard model within local DMFT, at least three to five bath levels must be taken into account [5]. An analogous five-orbital system would imply a total number of 20 to 30 levels, a virtually insurmountable and impractical task. The main point of our study is that an increasing number of correlated orbitals or sites requires a decreasing number of bath levels, so that, for the systems discussed in this work, overall sizes of 10 to 15 levels are adequate. Since computational times per iteration are of the order of minutes for 10 levels and a few hours for 15 levels, this implies that a large variety of strongly correlated materials of interest can be studied within ED DMFT. Moreover, this approach is applicable at large Coulomb energies and for full Hund exchange. Also, it is free of sign problems and statistical errors. We therefore conclude that finite-temperature ED DMFT is complementary to continuous-time QMC DMFT [22–24]. While the latter becomes computationally more demanding at low temperature because of statistical noise, the former gets more involved at high temperature due to the increasing number of excited states. Moreover, the low-temperature, low-energy properties are affected by finite-size limitations.

As discussed in Section 2, at each iteration step ED DMFT implies two projections: from the infinite lattice to the finite cluster, and back from the cluster to

the lattice. Mathematically, these projections assume that continuous and discrete real-energy spectra of the self-energy and Green’s function exist which have nearly identical representations along the Matsubara axis. To demonstrate the accuracy of this approach three criteria are available: (i) the convergence of key quantities, such as the self-energy, with increasing bath size, (ii) the accuracy of the discretization of the lattice bath Green’s function in terms of a cluster consisting of impurity and finite bath (the impurity may be formed by several sites), and (iii) the consistency with analogous results derived within QMC DMFT. In the case of three-band systems, calculations for two, three, and four bath levels per orbital have been performed. The comparisons for different bath sizes, the quality of the Green’s function discretization, and the comparison with QMC results illustrate that not only integrated quantities, such as orbital occupancies, but also dynamical features are usually well described with only two bath levels per orbital or site.

The successful application of ED DMFT involves two main ingredients: (i) the size of the Hilbert space and (ii) the discretization of the lattice via a finite cluster. The size of the Hilbert space determines the level spacing of excited states. This spacing must be sufficiently small, so that the low-energy behavior of the self-energy can be resolved. Of particular interest are correlation-induced effective mass enhancements, deviations from Fermi-liquid properties related to finite low-energy scattering rates, and the opening of Mott gaps. The accuracy of the discretization, on the other hand, depends in a crucial manner on the temperature used along the imaginary Matsubara axis. Decreasing this temperature implies increasing sensitivity to low-energy features of the lattice Green’s function which require baths of accordingly larger size. As the cluster Green’s function is always gapped, it cannot describe metallic behavior at very low energies. The examples discussed in the subsequent sections indicate that, to achieve accurate results with two bath levels per orbital or site, the Matsubara temperature should not be much lower than $T \approx 5, \dots, 10$ meV (assuming typical band widths $W \approx 2$ eV).

In the past, several groups have carried out multi-band or multi-site ED DMFT calculations at $T = 0$ [25–32]. In these studies, the impurity Green’s function is evaluated using the Lanczos method for the ground state while the DMFT iteration procedure and the discretization of the bath Green’s function are performed at a fictitious finite temperature to obtain sufficiently smooth distributions along the Matsubara axis. In the present work we focus mainly on ED at finite temperature in order to demonstrate the consistency of this approach with analogous results derived within continuous-time QMC DMFT. As in QMC, the temperature for the Matsubara grid is then the same as for the interacting impurity Green’s function. At low temperatures this function can in principle be obtained by generalizing the Lanczos scheme to finite

T . This approach, however, is rapidly plagued by the loss of orthogonality of excited states [21]. Here we make use of the Arnoldi algorithm [33] for large sparse matrices, which is ideally suited to evaluate those excited states that are physically important at low temperatures [20]. Whereas finite- T ED with full matrix diagonalization is feasible only up to about 8 levels [19] (maximum Hamiltonian dimension $N = 4900$), the Arnoldi scheme at present allows the consideration of 12 to 15 levels ($N \approx 10^6, \dots, 40 \times 10^6$) without significantly increased storage requirements [34]. Thus, materials involving up to five correlated orbitals or up to six correlated sites can now be investigated.

As the ED DMFT iterative procedure is carried out at imaginary frequencies, an additional step is required to extrapolate the converged Green's function and self-energy to real ω . In principle, these quantities can, of course, be evaluated directly at $\omega + i\gamma$, where γ denotes an artificial broadening. This aspect represents an important advantage compared to QMC DMFT, where real-energy spectra are usually obtained via the Maximum Entropy method [35]. On the other hand, the ED cluster properties are by definition discrete, so that the imaginary parts of the Green's function and self-energy consist of (broadened) δ -functions. These cluster spectra are adequate, for instance, if a metallic phase with many closely spaced peaks is compared to an insulating phase, which exhibits a clear gap. Mott transitions can therefore readily be identified via cluster spectra. To investigate finer features, such as the distinction between Fermi-liquid and non-Fermi-liquid behavior, it is useful (as in QMC) to analytically continue the lattice quantities from the Matsubara axis to real ω . Although this problem is known to be ill-posed, the important low-energy properties are usually rather insensitive to details of the extrapolation method, while large uncertainties exist in the incoherent region farther away from the Fermi energy. To illustrate some of these issues, cluster and lattice spectra will be compared in Section 3 for several systems.

Multi-orbital and multi-site Coulomb correlations are treated in this work within a common perspective since they share many computational aspects. The similarity becomes particularly evident by changing from the site basis in the case of cluster DMFT to a "molecular-orbital" or "plaquette" basis in which the onsite repulsion is converted into intra-orbital and inter-orbital Coulomb and exchange interactions. An interesting outcome of this parallel treatment is that characteristic physical phenomena, such as the transition from a Mott insulating phase at half-filling to non-Fermi-liquid and Fermi-liquid metallic phases at finite electron or hole doping, are found in multi-orbital materials as well as single-band models of high- T_c cuprates [34]. Thus, the existence of inter-orbital or inter-site interaction channels generates fascinating new physics not present in a single-band, single-site picture.

The outline of this paper is as follows. In Section 2 we review the finite-temperature ED DMFT approach for the evaluation of multi-band and multi-site Coulomb correlations. We also discuss the role of the two main ingredients in this approach, namely, the overall size of the Hilbert space of the finite cluster used to represent the infinite lattice, and the discretization of the bath Green's function. Section 3 presents the results for a variety of applications: (1) the degenerate three-band model, (2) several realistic three-band materials, such as $\text{Ca}_{2-x}\text{Sr}_x\text{RuO}_4$, LaTiO_3 , V_2O_3 , and Na_xCoO_2 , (3) the degenerate five-band model and its connection to iron-based pnictides and chalcogenides, the single-band Hubbard model for (4) the triangular lattice, (5) the square lattice, and (6) the honeycomb lattice. We have also applied finite- T ED within inhomogeneous DMFT [36] to study both single-site and non-local correlations in various heterostructures [37], but these will not be discussed in this paper. Section 4 provides a summary and outlook. In the Appendix the discretization of the bath Green's function is discussed in more detail for the degenerate three-band model and the square lattice. Energy units are eV unless noted otherwise.

2. ED DMFT FORMALISM

2.1. Multi-band Correlations

In this section we specify the details of ED DMFT appropriate for multi-band materials. In particular, we consider transition metal oxides, such as V_2O_3 , LaTiO_4 , and Ca_2RuO_4 , where, as a result of crystal field splitting, Coulomb correlations take place primarily within the partially occupied t_{2g} bands. In addition to these three-band systems, we also consider the more general case in which all five d bands are relevant near the Fermi level. This applies to ordinary transition metals, oxides such as MnO or LaMnO_3 , and iron pnictides and chalcogenides, such as FeAsLaO and FeSe . We focus on the influence of onsite Coulomb correlations and neglect spatial fluctuations. Within this multi-band single-site DMFT approach the complex self-energy accounts for dynamical correlation effects, such as spectral weight transfer between low-energy and high-energy regions and quasi-particle broadening, while its momentum dependence is neglected.

The single-particle properties are assumed to be given in terms of an effective tight-binding Hamiltonian $t(\mathbf{k})$ which is derived from a fit to results obtained within density functional theory (DFT). The interacting Hamil-

tonian is given by:

$$\begin{aligned}
H = & \sum_{mn\mathbf{k}\sigma} t_{mn}(\mathbf{k})c_{\mathbf{k}m\sigma}^+c_{\mathbf{k}n\sigma} + \sum_{im} Un_{im\uparrow}n_{im\downarrow} \\
& - \sum_{im\sigma} \mu n_{im\sigma} + \sum_{im<m'\sigma\sigma'} (U' - J\delta_{\sigma\sigma'})n_{im\sigma}n_{im'\sigma'} \\
& - \sum_{im\neq m'} J[c_{im\uparrow}^+c_{im\downarrow}c_{im'\downarrow}^+c_{im'\uparrow} + c_{im\uparrow}^+c_{im\downarrow}^+c_{im'\uparrow}c_{im'\downarrow}],
\end{aligned} \tag{1}$$

where $c_{im\sigma}^{(+)}$ are annihilation (creation) operators for electrons on site i in orbital m with spin σ and $n_{im\sigma} = c_{im\sigma}^+c_{im\sigma}$. $c_{\mathbf{k}m\sigma}^{(+)}$ are the corresponding Fourier components. μ is the chemical potential and the intra-orbital and inter-orbital Coulomb energies are denoted by U and U' , respectively. The exchange integral is J , where $U' = U - 2J$ because of rotational invariance [38].

For simplicity we limit the discussion to systems in which non-diagonal components of the density of states vanish for symmetry reasons. The diagonal elements of the lattice Green's function are then given by

$$G_m(i\omega_n) = \sum_{\mathbf{k}} [i\omega_n + \mu - t(\mathbf{k}) - \Sigma(i\omega_n)]_{mm}^{-1}, \tag{2}$$

where $\omega_n = (2n + 1)\pi/\beta$ are Matsubara frequencies ($\beta = 1/T$), and Σ is the self-energy matrix. Since local Coulomb interactions preserve the symmetry properties of G , Σ is also diagonal in orbital space, with elements $\Sigma_m(i\omega_n)$. We consider only paramagnetic systems, so that the spin index of G and Σ can be omitted. Note that, because of the non-diagonal nature of $t(\mathbf{k})$, the components of G are influenced by all components of Σ . In the limit of large ω_n , the lattice Green's function components take the simple form

$$G_m(i\omega_n) = [i\omega_n + \mu - \epsilon_m - \Sigma_m(i\omega_n)]^{-1}, \tag{3}$$

where $\epsilon_m = [\sum_{\mathbf{k}} t(\mathbf{k})]_{mm}$.

For the purpose of the quantum impurity calculation within DMFT it is necessary to remove the self-energy from the central site in order to avoid double-counting of Coulomb interactions. This step yields the so-called bath Green's function [39]

$$G_{0,m}(i\omega_n) = [G_m(i\omega_n)^{-1} + \Sigma_m(i\omega_n)]^{-1}. \tag{4}$$

Note that G_0 is not the non-interacting Green's function obtained from Eq. (2) for $\Sigma = 0$. Instead, G_0 accounts for the electronic motion from the central site throughout the lattice back to the central site, where Σ is present at all sites except the central one.

Within ED DMFT the infinite lattice surrounding the central site is approximated via a bath of finite size. Thus, the above Green's function is approximated in terms of an Anderson impurity model for a cluster consisting of n_c impurity levels $\epsilon_{m=1,\dots,n_c}$ and n_b bath levels $\epsilon_{k=n_c+1,\dots,n_s}$, which hybridize via hopping matrix elements V_{mk} . Here, $n_s = n_c + n_b$ defines the total number

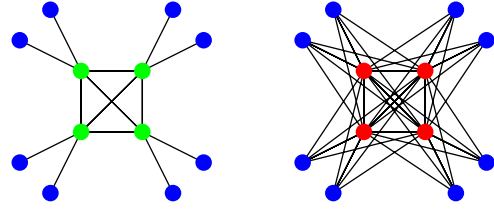


FIG. 1: (Color online) Left panel: Impurity bath interactions within diagonal basis for four orbitals. Green dots: impurity levels ($m = 1, \dots, 4$); blue dots: bath levels ($k = 5, \dots, 12$). Each impurity orbital interacts with its own bath via hopping terms V_{mk} . The impurity orbitals interact only via Coulomb and exchange terms since the system is diagonal in this basis. Right panel: Non-diagonal mixed basis involving impurity sites ($i = 1, \dots, 4$) (red dots) and molecular-orbital bath levels (blue dots). Interactions among sites are determined by single-particle hopping, whereas the Coulomb interaction is purely onsite. Bath levels now hybridize with all impurity sites. The interactions indicated in the left and right panels are equivalent, since they differ only by a unitary transformation among impurity orbitals.

of cluster levels. The bath levels ϵ_k and hopping terms V_{mk} may be viewed as auxiliary quantities to achieve an optimal representation of the lattice bath Green's function in terms of a finite cluster. (The term ‘‘cluster’’ here refers to the finite set of impurity and bath levels and should not be confused with the ‘‘correlated impurity cluster’’ discussed in the next subsection.) Thus,

$$G_{0,m}(i\omega_n) \approx G_{0,m}^{cl}(i\omega_n), \tag{5}$$

where

$$G_{0,m}^{cl}(i\omega_n) = \left(i\omega_n + \mu - \epsilon_m - \sum_{k=n_c+1}^{n_s} \frac{|V_{mk}|^2}{i\omega_n - \epsilon_k} \right)^{-1}. \tag{6}$$

(The bath levels are defined relative to μ .) Since the lattice Green's function is diagonal in the orbital index, we can assume that each impurity orbital couples only to its own bath. For instance, for $n_c = 4$ and $n_b = 8$ (i.e., two bath levels per impurity orbital), only the elements $V_{m,m+4}$, $V_{m,m+8}$, and their transpose elements are nonzero. All other elements vanish. These interactions are schematically indicated in the left panel of Figure 1. Details concerning the discretization indicated in Eq. (6) will be discussed in Section 2.4.

Adding the onsite Coulomb interactions to the single-particle Hamiltonian specified by ϵ_m , ϵ_k , and V_{mk} , the interacting cluster Green's function at finite T is derived

from the expression [20, 21]

$$\begin{aligned}
G_m^{cl}(i\omega_n) &= \frac{1}{Z} \sum_{\nu\mu} e^{-\beta E_\nu} \left(\frac{|\langle \mu | c_{m\sigma}^+ | \nu \rangle|^2}{i\omega_n + E_\mu - E_\nu} \right. \\
&\quad \left. + \frac{|\langle \mu | c_{m\sigma} | \nu \rangle|^2}{i\omega_n + E_\nu - E_\mu} \right) \\
&= \frac{1}{Z} \sum_{\nu} e^{-\beta E_\nu} [G_{m,\nu}^{cl+}(i\omega_n) + G_{m,\nu}^{cl-}(i\omega_n)],
\end{aligned} \tag{7}$$

where E_ν and $|\nu\rangle$ denote the eigenvalues and eigenvectors of the full Hamiltonian, and $Z = \sum_{\nu} \exp(-\beta E_\nu)$ is the partition function. $G_{m,\nu}^{cl\pm}(i\omega_n)$ are Green's functions derived from the excited states $|\nu\rangle$. G^{cl} satisfies the same symmetry properties as G and G_0 , so that it is also diagonal in orbital space. The orbital components of the cluster self-energy can be obtained from an expression analogous to Eq. (4):

$$\Sigma_m^{cl}(i\omega_n) = G_{0,m}^{cl}(i\omega_n)^{-1} - G_m^{cl}(i\omega_n)^{-1}. \tag{8}$$

The key assumption in DMFT is that this cluster self-energy is a physically reasonable representation of the lattice self-energy. Thus,

$$\Sigma_m(i\omega_n) = \Sigma_m^{cl}(i\omega_n), \tag{9}$$

so that, as a result of Eq. (5),

$$G_m(i\omega_n) \approx G_m^{cl}(i\omega_n). \tag{10}$$

In the next iteration step, these diagonal self-energy components are used as input in the lattice Green's function, Eq. (2). The iteration cycle then has the schematic form

$$\begin{aligned}
\varepsilon_m, \varepsilon_k, V_{mk} &\rightarrow G_{0,m}^{cl}, G_m^{cl}, \Sigma_m^{cl} \\
&\rightarrow \Sigma_m, G_m, G_{0,m} \\
&\rightarrow \varepsilon_m, \varepsilon_k, V_{mk}.
\end{aligned} \tag{11}$$

In practice, the initial cluster parameters ε_m , ε_k , and V_{mk} are obtained from a fit of the uncorrelated lattice Green's function or from a previous solution for weaker interaction parameters, other doping concentrations, etc.

The ED DMFT self-consistency procedure involves at each iteration two projections: from lattice to cluster, and back from cluster to lattice. By definition, lattice quantities such as G , G_0 , and Σ have continuous spectra at real energies, while the analogous cluster quantities, G^{cl} , G_0^{cl} , and Σ^{cl} are discrete. In this sense, the cluster quantities are never equal to the corresponding lattice versions, except for an infinite number of bath levels. The advantage of working at finite T is that, along the Matsubara axis at not too low temperatures, both sets of quantities become rather smooth, so that they can be meaningfully compared, even if only a finite number of bath levels is employed.

Mathematically, the lattice-to-cluster and cluster-to-lattice projections in Eqs. (5) and (9) imply that continuous and discrete real-energy spectra exist which have

nearly identical representations along the Matsubara axis. In particular, the success of ED DMFT as a method for describing strongly correlated properties depends crucially on the accuracy of the discretization of G_0 , Eq. (5), which, in turn, depends on bath size and temperature. This will be discussed in more detail in Section 2.4. The quality of this discretization will also be illustrated in Section 3 for a variety of realistic systems. Additional details concerning the finite-temperature multi-orbital ED DMFT approach can be found in Ref. [20].

Comparing the ED DMFT formalism outlined above to QMC DMFT, it is clear that both schemes involve additional errors beyond the basic single-site DMFT approximation: In the case of ED, the bath Green's function G_0 is discretized, so that the interacting impurity Green's function suffers from finite-size effects. In the case of QMC, the discretization is avoided, but the interacting impurity Green's function suffers from errors due to statistical uncertainties. As a result, the limit of very low temperatures and energies is inaccessible to both schemes.

We also note that the iterative procedure indicated in Eq. (12) is not unique. For instance, in the definition of the cluster self-energy, Eq. (8), one could replace $G_{0,m}^{cl}$ by the more accurate lattice function $G_{0,m}$. Nevertheless, Eq. (8) is found to yield a more reliable convergence towards a self-consistent solution. In addition, instead of finding the cluster parameters ε_m , ε_k , and V_{mk} in the $(i+1)^{th}$ iteration step from the actual lattice bath Green's function $G_{0,m}$ as indicated in Eq. (5), it is more convenient to employ an admixture

$$G_{0,m}^{cl,(i+1)} \approx \alpha G_{0,m} + (1-\alpha) G_{0,m}^{cl,(i)}, \tag{12}$$

where $G_{0,m}^{cl,(i)}$ is the cluster bath Green's function of the previous iteration step and $\alpha \approx 0.5$. With these definitions, 5 to 10 iterations are usually sufficient to achieve convergence.

As mentioned above, we have assumed so far that the local Green's function and self-energy are diagonal in the orbital basis. Complex lattice geometries, however, can give rise to non-diagonal components which require a suitable generalization of the above formalism. This will be briefly addressed at the end of the next subsection.

2.2. Multi-Site Correlations

Let us consider now a single-band Hubbard model and include spatial correlations among a finite number of sites (n_c). To be specific, we limit the discussion to two-dimensional systems, such as the square lattice with isotropic nearest and next-nearest neighbor coupling, and the triangular and honeycomb lattices with isotropic nearest-neighbor hopping integrals. The Coulomb interaction within the band is assumed to be a purely on-site

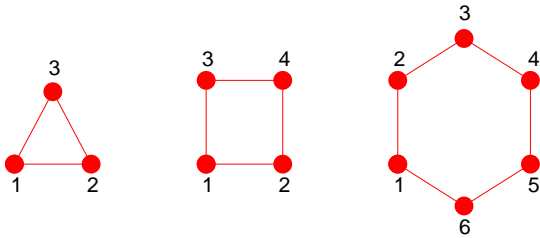


FIG. 2: (Color online) Unit cells within CDMFT for triangular, square, and honeycomb lattices.

interaction. Models of this kind are believed to capture important features related to short-range correlations in high- T_c cuprate superconductors, organic molecular crystals, and in graphene. The Hamiltonian of the system is given by

$$H = - \sum_{\langle ij \rangle \sigma} t_{ij} (c_{i\sigma}^\dagger c_{j\sigma} + \text{H.c.}) + U \sum_i n_{i\uparrow} n_{i\downarrow} - \sum_{i\sigma} \mu n_{i\sigma} \quad (13)$$

where the sum in the first term extends up to first or second neighbors.

Within the cluster extension [11] of DMFT (CDMFT) the interacting lattice Green's function in the cluster site basis may be written as

$$G_{ij}(i\omega_n) = \sum_{\mathbf{k}'} [i\omega_n + \mu - t(\mathbf{k}') - \Sigma(i\omega_n)]_{ij}^{-1}, \quad (14)$$

where the \mathbf{k}' sum covers the reduced Brillouin Zone and $t(\mathbf{k}')$ denotes the hopping matrix for the superlattice. Σ_{ij} represents the cluster self-energy matrix. The site labels for the three lattices are indicated in Figure 2. For the purpose of the ED calculation, it is convenient to change from the non-diagonal site basis to a “molecular-orbital” basis, in which the lattice Green's function is diagonal. For the triangular lattice, the diagonal components G_m are given by:

$$\begin{aligned} G_1 &= G_{11} + 2G_{12} \\ G_2 = G_3 &= G_{11} - G_{13}. \end{aligned} \quad (15)$$

For the square lattice, the diagonal components are:

$$\begin{aligned} G_{1,2} &= G_{11} \pm 2G_{12} + G_{14} \\ G_3 = G_4 &= G_{11} - G_{14}. \end{aligned} \quad (16)$$

For the honeycomb lattice, they are given by:

$$\begin{aligned} G_{1,2} &= (G_{11} + 2G_{13}) \pm (G_{14} + 2G_{12}) \\ G_{3,4} = G_{5,6} &= (G_{11} - G_{13}) \pm (G_{14} - G_{12}). \end{aligned} \quad (17)$$

The cluster self-energy can be diagonalized in the same

manner, with elements Σ_m . In the molecular-orbital basis, the lattice Green's function takes the form:

$$G_m(i\omega_n) = \sum_{\mathbf{k}'} [i\omega_n + \mu - t'(\mathbf{k}') - \Sigma(i\omega_n)]_{mm}^{-1}, \quad (18)$$

where $t'(\mathbf{k}') = \bar{T}^{-1} t(\mathbf{k}') \bar{T}$ and $\bar{T} = [\bar{T}_{im}]$ denotes the unitary transformation from the site basis to the molecular-orbital basis. For the triangular, square and honeycomb lattices, the matrices \bar{T} and the molecular-orbital components $\rho_m(\omega)$ of the uncorrelated density of states can be found in Refs. [40–42]. The asymptotic behavior of the Green's function components is given by

$$G_m(i\omega_n) = [i\omega_n + \mu - \varepsilon_m - \Sigma_m(i\omega_n)]^{-1}, \quad (19)$$

where $\varepsilon_m = [\sum_{\mathbf{k}'} t'(\mathbf{k}')]_{mm}$.

Evidently, with the transformation from lattice sites to molecular orbitals, the ED CDMFT procedure becomes analogous to the multi-orbital formalism discussed in the previous subsection. In particular, the removal of the self-energy from the “impurity cluster” yields the bath Green's function components $G_{0,m}(i\omega_n)$ given by Eq. (4), which are discretized according to Eq. (6) by replacing the host continuum by a finite set of levels ε_k . Thus, cluster molecular orbitals and bath form a “supercluster” of size $n_s = n_c + n_b$ whose many-body properties can be solved exactly. (In the following we use the term “cluster” mainly for the unit cells depicted in Figure 2. From the context it will be clear whether the larger supercluster is implied instead.)

Assuming independent baths for the impurity molecular orbitals, the hybridization interaction takes the form as schematically indicated in the left diagram of Figure 1 for the case $n_c = 4$. The advantage of this diagonal basis is that, as in the multi-orbital case discussed in the previous subsection, the bath Green's function components $G_{0,m}^{cl}(i\omega_n)$ can be discretized independently, rather than fitting the non-diagonal Green's function matrix $G_{0,ij}^{cl}(i\omega_n)$ in the site basis in one step [30, 40].

The evaluation of the interacting cluster Green's function G^{cl} can be carried out within the diagonal molecular-orbital basis, yielding the components $G_m^{cl}(i\omega_n)$ defined in Eq. (8). In this basis, the onsite Coulomb interaction is a non-diagonal matrix, with intra-orbital and inter-orbital elements that are analogous to the Coulomb and exchange interactions of the single-site, multi-orbital systems discussed in the previous subsection. For instance, in the case of a 2×2 cluster representing a square lattice, one finds $\langle m_1 m_2 || m_3 m_4 \rangle = U/4$ for 64 of the 256 matrix elements, where $U = \langle ii || ii \rangle$ is the on-site Coulomb interaction. All other elements vanish. An equivalent scheme consists in transforming the cluster molecular orbitals back to the site basis, by using the transformation \bar{T} introduced above. Thus, the bath molecular-orbital levels remain unchanged and the Coulomb interaction is purely onsite. In this mixed site molecular-orbital picture the

non-diagonal cluster Green's function is evaluated from the expression

$$\begin{aligned}
 G_{ij}^{cl}(i\omega_n) &= \frac{1}{Z} \sum_{\nu\mu} e^{-\beta E_\nu} \left(\frac{\langle \nu | c_{i\sigma} | \mu \rangle \langle \mu | c_{j\sigma}^\dagger | \nu \rangle}{i\omega_n + E_\mu - E_\nu} \right. \\
 &\quad \left. + \frac{\langle \nu | c_{i\sigma}^\dagger | \mu \rangle \langle \mu | c_{j\sigma} | \nu \rangle}{i\omega_n + E_\nu - E_\mu} \right) \\
 &= \frac{1}{Z} \sum_{\nu} e^{-\beta E_\nu} [G_{ij,\nu}^{cl+}(i\omega_n) + G_{ij,\nu}^{cl-}(i\omega_n)],
 \end{aligned} \tag{20}$$

where $G_{ij,\nu}^{cl\pm}(i\omega_n)$ are Green's functions corresponding the excited state $|\nu\rangle$. Since G_{ij}^{cl} satisfies the same symmetry properties as G_{ij} , it is diagonal within the molecular-orbital basis, whose elements G_m^{cl} coincide with those derived via Eq. (8). Within the non-diagonal site basis, the cluster bath hybridization takes the form indicated in the right diagram of Figure 1. The molecular-orbital bath levels do not mix within this representation, but hybridize with all cluster sites. Further details concerning the finite-temperature multi-site ED DMFT approach are provided in Ref. [41].

The lattice examples considered above are special in the sense that a diagonal molecular-orbital basis exists. More general cases, such as the non-isotropic triangular or square lattices, require suitable generalizations of the above formalism. As long as direct coupling between bath levels is excluded, the most general hybridization between impurity and bath levels is still represented by the right-hand diagram in Figure 1, but the hopping terms V_{ik} obey weaker symmetry relations than before. As a result, the back-transformation to the molecular-orbital basis does not yield a diagonal Green's function. Because of the off-diagonal elements, the diagonal components can no longer be fitted independently of one another. Instead, the full bath Green's function matrix (or a suitable subblock) must be discretized in a single sweep [27, 29–31, 43, 44]. Similarly, complex lattice geometries in multi-band single-site cases can give rise to non-diagonal inter-orbital components. Since the impurity bath hybridization is then also of the form as indicated in the right diagram of Figure 1, the discretization must be carried out in one step, rather than using independent fits of the $G_{0,m}$ as in the diagonal case.

2.3. Size of Hilbert Space

An important criterion for the accuracy of ED DMFT is the level spacing related to the finite size of the cluster consisting of impurity and bath. The dimension of the Hilbert space for $n_s = n_c + n_b$ cluster levels is 2^{2n_s} . Since different spin sectors of the Hamiltonian do not couple, the largest sector for $n_s = 9$ has dimension $N = (9!/(4!5!))^2 = 15876$. For $n_s = 12$, the dimension is $(12!/(6!6!))^2 = 853776$, while for $n_s = 15$, it is

$(15!/(7!8!))^2 = 41409225$. Fortunately, the cluster Hamiltonian is extremely sparse, with typically no more than 20 to 30 finite off-diagonal elements per row. Thus, using 32 parallel processors for $n_s = 15$, storage requirements per processor are about the same as for full matrix diagonalization for $n_s = 8$ levels ($N = 4900$). Moreover, because of the Boltzmann factor in the cluster Green's function, Eqs. (8) and (21), only a limited number of excited states is required at finite T . The quantum impurity calculation can therefore be carried out very efficiently by using the Arnoldi algorithm [33], which generates a finite number of eigenvalues and eigenvectors of large sparse matrices. The contributions to the cluster Green's function are then given by a superposition of excited state Green's functions $G_{m,\nu}^{cl\pm}(i\omega_n)$ or $G_{ij,\nu}^{cl\pm}(i\omega_n)$ which can readily be calculated by applying the Lanczos method.

The key point here is that for $n_s = 9, \dots, 15$ the components of the interacting cluster Green's function, if evaluated at real ω , contain vastly more poles than their non-interacting counterparts, $G_{0,m}^{cl}$. Thus, even if a particular impurity level ε_m couples only to two bath levels ε_k , the indirect coupling to the remaining baths via internal Coulomb and exchange interactions within the impurity ensures a nearly continuous spectral distribution. In the case of multi-site correlations, the diagonal molecular-orbital basis implies many intra-orbital and inter-orbital Coulomb and exchange-like terms, whereas in the non-diagonal site basis the coupling between baths stems from the single-particle hopping between cluster sites.

Dynamical mean field theory may be viewed as a scheme for evaluating the complex self-energy, which defines the redistribution of spectral weight arising from Coulomb interactions. According to Eq. (8), the cluster self-energy is governed by the spectral details of the interacting cluster Green's function. Thus, for $n_s = 9, \dots, 15$ the nearly continuous spectral distributions of the components G_m^{cl} ensure accordingly smooth distributions of Σ_m^{cl} . Moreover, because of the high quality of these functions along the Matsubara axis, analytic continuation to real ω close to the Fermi energy is usually found to be rather stable. In principle, the cluster Green's function and self-energy can be evaluated close to the real-energy axis which is a crucial advantage compared to QMC DMFT. On the other hand, as pointed out above, at each iteration in ED DMFT the cluster self-energy (with its discrete level spectrum) is assumed to provide a physically reasonable representation of the continuous lattice self-energy, in the sense that along the Matsubara axis both are nearly identical. Thus, as in QMC DMFT, analytic continuation of the self-energy is desirable and can be carried out using various methods. (A detailed discussion of the analytic continuation of the self-energy is given in Ref. [45].) Since the single-particle properties are known at real energies, no further approximations

are then required. This should be contrasted to analytic continuation of the lattice Green's function, which implies continuation of both self-energy and single-particle features. (The limit of weak interactions makes the difference between these two methods particularly striking.)

For some of the examples discussed in the next section, we have employed the routine *ratint* [46] for the extrapolation of the self-energy and lattice Green's function to real ω . Typically, up to a few hundred Matsubara points are used, with a small frequency-dependent broadening. This procedure usually yields reliable results at low energies, while considerable uncertainties arise in the incoherent region at larger energies.

The multi-orbital and multi-site scenarios discussed above differ greatly from the simpler single-band, single-site case. Even if at some finite temperature the lattice bath Green's function can be discretized accurately via a non-interacting cluster Green's function using few bath levels, the small cluster size yields a very coarse level spectrum. It is therefore essential to include more bath levels so that the larger Hilbert space guarantees better energy resolution. Nevertheless, it has been shown that integrated quantities, such as the critical Coulomb energies $U_{c1,c2}$ determining the T/U phase diagram for the Mott transition at half-filling, are already well converged using only 3 or 4 bath levels [19] (see also [21]).

2.4. Bath Discretization

The second important criterion for the accuracy of ED DMFT concerns the projection of the bath Green's function components $G_{0,m}(i\omega_n)$ onto to a finite cluster, as indicated by the discretization in Eqs. (5) and (6). Evidently, the quality of this discretization depends sensitively on temperature and bath size. Along the Matsubara axis the spectrum of $G_{0,m}(\omega)$ is effectively sampled with Lorentzian functions of width $\omega_n = (2n + 1)\pi T$:

$$\text{Im } G_{0,m}(i\omega_n) = \frac{1}{\pi} \int d\omega \frac{\omega_n}{\omega^2 + \omega_n^2} \text{Im } G_{0,m}(\omega). \quad (21)$$

Thus, choosing a very low temperature gives rise to fine structure in $G_{0,m}(i\omega_n)$ that can be fitted only with a sufficiently large number of bath levels. For the description of multi-band or multi-site correlations with no more than two bath levels per impurity orbital it is therefore important to employ a Matsubara grid for not too low T . As will be discussed in more detail in the next section, applications to a variety of multi-band and multi-site correlation problems suggest that a temperature in the range $T \approx 5, \dots, 20$ meV (for typical band widths of the order of $W = 2$ eV) permits discretizations of reasonable accuracy. (Note that at very small ω_n a sufficiently large number of \mathbf{k} points must be used to get accurate lattice Green's functions, Eqs. (2) and (14). See also Eq. (21).)

To determine the bath levels ε_k and hopping terms V_{mk} we minimize the difference

$$\text{Diff}_m = \sum_{n=0}^M W_n |G_{0,m}(i\omega_n) - G_{0,m}^{cl}(i\omega_n)|^2, \quad (22)$$

where $M \approx 2^{10}$ is the total number of Matsubara points and the weight function $W_n = 1/\omega_n$ is introduced to give more weight to the low-frequency region [26]. Since $G_{0,m}^{cl} \rightarrow 1/i\omega_n$ at large ω_n , it is appropriate to optimize the low-energy region. To carry out the above fit, we use the routine *minimize* provided in Ref. [5]. To start the iterative procedure, we use bath parameters obtained for the uncorrelated system, or from a converged solution for nearby Coulomb and exchange energies. The resulting ε_k and V_{mk} are usually very stable against (not too large) variations of initial conditions.

We have also tested other weight functions, such as $W_n = 1$ and $W_n = 1/\omega_n^2$, as well as minimization of [26]

$$\text{Diff}'_m = \sum_{n=0}^M W_n |G_{0,m}(i\omega_n)^{-1} - G_{0,m}^{cl}(i\omega_n)^{-1}|^2, \quad (23)$$

which represents the discretization of the lattice hybridization function

$$\Delta_m(i\omega_n) = i\omega_n + \mu - \varepsilon_m - G_{0,m}(i\omega_n)^{-1} \quad (24)$$

via the corresponding cluster expression, i.e., the last term in Eq. (6). Thus,

$$\Delta_m(i\omega_n) \approx \Delta_m^{cl}(i\omega_n) = \sum_{k=n_c+1}^{n_s} \frac{|V_{mk}|^2}{i\omega_n - \varepsilon_k}, \quad (25)$$

so that

$$\text{Diff}'_m = \sum_{n=0}^M W_n |\Delta_m(i\omega_n) - \Delta_m^{cl}(i\omega_n)|^2. \quad (26)$$

It can easily be shown that, in the limit of large ω_n ,

$$|G_{0,m}(i\omega_n) - G_{0,m}^{cl}(i\omega_n)| \rightarrow \frac{1}{\omega_n^2} |\Delta_m(i\omega_n) - \Delta_m^{cl}(i\omega_n)|. \quad (27)$$

Thus, minimization of $|G - G^{cl}|$ ensures greater accuracy at small ω_n than minimization of $|1/G - 1/G^{cl}|$. Experience has shown that the ED DMFT iteration procedure, using the distance function defined in Eq. (22) with $W_n = 1/\omega_n$, yields reliable and efficient convergence. Nonetheless, as discussed in the Appendix, other weight functions, as well as utilization of Eq. (23), also provide accurate discretization of the bath Green's function. (For a recent discussion of various choices of weight functions, mainly for the one-dimensional Hubbard model, see Ref. [32].)

In principle, the asymptotic behavior of $G_{0,m}(i\omega_n)$ and $G_{0,m}^{cl}(i\omega_n)$ is governed by the impurity levels ε_m ,

which follow from the single-particle properties of the multi-band or multi-site Hamiltonians, as indicated in Eqs. (3) and (19). Since this asymptotic behavior is only weakly affected by the precise value of ε_m , a more accurate discretization of $G_{0,m}(i\omega_n)$ in the low-frequency region may be achieved by allowing ε_m to vary. In effect, ε_m is then included among the auxiliary parameters used to obtain the optimal fit of the lattice bath Green's function $G_{0,m}(i\omega_n)$ via the cluster bath Green's function $G_{0,m}^{cl}(i\omega_n)$, even though this implies a (small) inconsistency between cluster and lattice properties. As a consequence of the finite bath size, slight inconsistencies of this kind are an intrinsic feature of ED quantum impurity calculations. They appear, for example, in the orbital occupancies, as calculated from the cluster and lattice Green's functions. In most cases we have found the freely determined impurity levels to be very close to the nominal bulk values specified in Eqs. (3) and (19). Thus, the variation of ε_m is not essential for the discretization procedure.

For a typical situation with two bath levels per impurity orbital, each complex function $G_{0,m}(i\omega_n)$ is then fitted with five parameters: two bath levels ε_k , two hopping terms V_{mk} , and ε_m . For instance, in the case of 2×2 clusters representing the square lattice with $n_c = 4$ and $n_b = 8$, we have a total of 15 fit parameters for the three independent Green's function components (12 fit parameters for fixed ε_m). Naturally, this parameter set provides a more accurate bath discretization than in the site basis, where for symmetry reasons only four fit parameters are usually taken into account. In the special case of particle-hole symmetry at half-filling, the diagonal basis employs 8 to 10 parameters, compared to 2 parameters in the site basis, unless additional hybridization terms are incorporated as indicated in the right panel of Figure 1.

3. RESULTS AND DISCUSSION

3.1. Degenerate Three-Band Model

As a first application of multi-band ED DMFT we consider a three-band Hubbard model consisting of identical subbands with a Bethe lattice density of states ($t = 1/2$, band width $W = 2$). The subbands are coupled only via Coulomb and exchange interactions. Single-particle hybridization among bands is neglected. Despite its simplicity, this model is highly non-trivial. As shown by Werner *et al.* [47], it exhibits metal insulator transitions at integer occupancies and a spin freezing transition within an intermediate range of occupancies. At the latter transition, the self-energy changes from Fermi-liquid to non-Fermi-liquid behavior and the spin-spin correlation function changes from Pauli to Curie-Weiss behavior. We discuss this model here in some detail in order to demonstrate the convergence of the ED results with

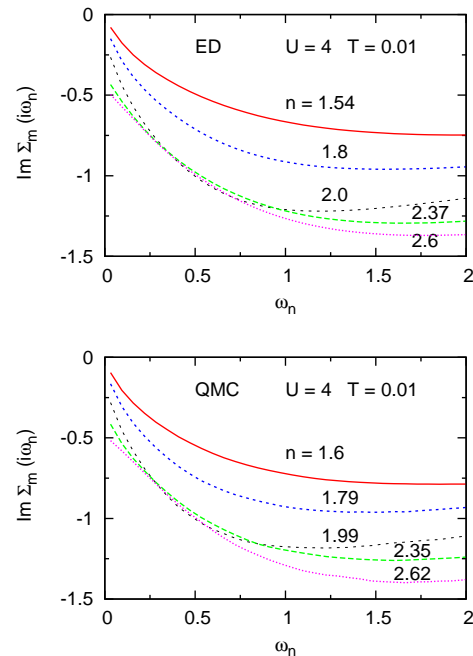


FIG. 3: (Color online) Self-energy of degenerate three-band model for $U = 4$, $J = U/6$, $T = 0.01$ at several occupancies. Upper panel: ED DMFT results for $n_s = 12$ (3 bath levels per impurity orbital). Lower Panel: continuous-time QMC DMFT results for similar occupancies (adapted from Figure 3 of [47]).

bath size, the quality of the discretization of the bath Green's function G_0 , and the consistency with analogous continuous-time QMC results reported in Ref. [47]. We also discuss briefly that, for sufficiently large Hund's rule coupling, the self-energy reveals a collective mode due to spin fluctuations, which leads to a pseudogap in the density of states. A similar collective mode is found in the five-band model discussed in Section 3.3.

Figure 3 (upper panel) shows the subband self-energy as a function of Matsubara frequency for various occupancies. The cluster size is $n_s = 12$, with three bath levels per orbital. Full Hund exchange is used, with $J = U/6$, and the Coulomb energy $U = 2W = 4$ is chosen so that at half-filling the system is a Mott insulator ($U_c \approx 1.5$ [48]). The corresponding QMC results are given in the lower panel for similar occupancies. The comparison shows that there is nearly quantitative agreement between the ED and QMC results, in particular, in the important low-energy region. At $n \approx 1.6$, the system is a Fermi liquid, with $\text{Im} \Sigma_m(i\omega_n) \rightarrow \omega_n$ in the limit of small ω_n . Near $n \approx 2$, $\text{Im} \Sigma_m$ begins to exhibit a finite onset as a result of local-moment formation. At larger occupancies, this onset continues to increase until the Mott phase is reached and, at half-filling, $\text{Im} \Sigma_m(i\omega_n) \rightarrow 1/\omega_n$ at small ω_n . The results in Figure 3 are for $T=0.01$. Similarly good agreement is obtained for $T = 0.005$ (not

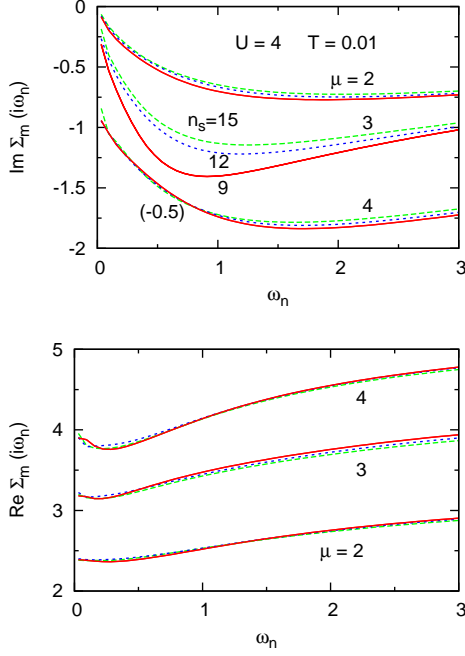


FIG. 4: (Color online) Convergence of self-energy for three-band model with bath size at different chemical potentials. Solid red curves: $n_s = 9$, dashed blue curves: $n_s = 12$, long-dashed green curves: $n_s = 15$, corresponding to two, three, and four bath levels per impurity orbital, respectively. For clarity, the results in the upper panel for $\text{Im } \Sigma_m$ at $\mu = 4$ are shifted down by 0.5. $U = 4$, $J = U/6$, $T = 0.01$.

shown here).

Analogous results for only two bath levels per orbital ($n_s = 9$) show qualitatively the same behavior as for $n_s = 12$. In fact, at $\mu = 2$ ($n \approx 1.6$) and $\mu = 4$ ($n \approx 2.5$), the self-energies are nearly the same as for the larger cluster. Only in the transition region near $\mu = 3$ ($n \approx 2.0$), larger differences are found, including a stronger dependence on temperature. To illustrate the convergence of the self-energy with bath size more systematically, we show in Figure 4 results of ED DMFT calculations for $n_s = 9, 12$, and 15. The calculations for 2 and 3 bath levels per orbital are carried out at $T = 0.01$, whereas for computational reasons the ones for $n_s = 15$ are performed at $T = 0$ in the evaluation of the cluster Green's function, Eq. (8). The Matsubara grid employed in the DMFT self-consistency procedure corresponds to $T = 0.01$ in all cases. For $\mu = 2$ and 4, both the real and imaginary parts of Σ_m are in good agreement for the different cluster sizes. In particular, in the Fermi liquid range for $\mu = 2$, $\text{Im } \Sigma_m \sim \omega_n$ in the limit of small ω_n , with an effective mass enhancement of $m^*/m \approx 3$. In contrast, for $\mu = 4$, $\text{Im } \Sigma_m$ approaches a constant, reflecting the finite scattering rate due to the presence of frozen moments. For $\mu = 3$, the increase from $n_s = 9$ to 15 is seen to shift the minimum of $\text{Im } \Sigma_m(i\omega_n)$ to larger

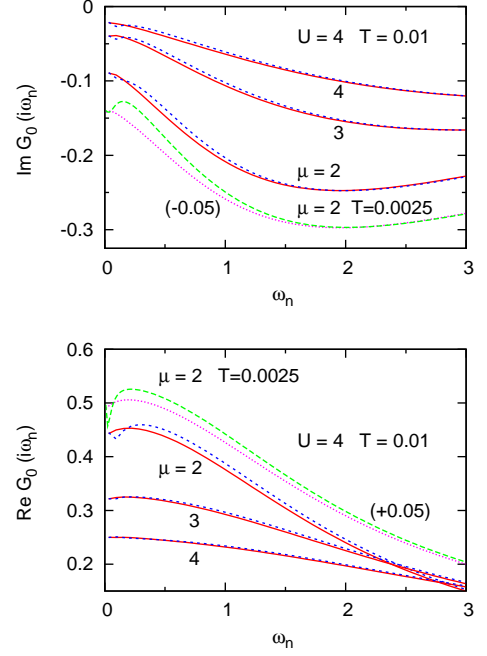


FIG. 5: (Color online) Discretization of bath Green's function: lattice $G_{0,m}(i\omega_n)$ (solid red curves) and cluster $G_{0,m}^{cl}(i\omega_n)$ (dashed blue curves) for 2 bath levels per impurity orbital ($n_s = 9$) at several chemical potentials; $U = 4$, $J = U/6$, $T = 0.01$. The dashed (magenta and green) curves show the fit for $\mu = 2$ at $T = 0.0025$. (For clarity the latter results are shifted vertically by ± 0.05).

ω_n and to make it more shallow, with a larger change from $n_s = 9$ to 12 than from $n_s = 12$ to 15. The reason for the stronger variation with bath size at $\mu = 3$ is that this chemical potential nearly coincides with the phase boundary of the spin freezing transition. Thus, small variations due to the finite cluster size can give rise to larger changes of the self-energy.

We point out that the self-energy shown in Figure 4 as a function of bath size does not exhibit any oscillatory behavior related to the even or odd number of bath levels per impurity orbital. This kind of dependency on bath size occurs in more special cases, such as particle-hole symmetric bands at half-filling. (See, for example, the two-band model discussed in Ref. [19].) The presence or absence of bath levels at the Fermi energy then tends to favor metallic or insulating behavior, leading to a slow convergence with the number of bath levels. In the present degenerate three-band model, the bath levels away from half-filling do not obey any particular symmetry rules, so that oscillatory variation with bath size does not arise.

As discussed in the previous section, a crucial criterion for the convergence with bath size in ED DMFT is the quality of the discretization of the bath Green's function $G_{0,m}(i\omega_n)$, Eq. (4), via the cluster Green's function

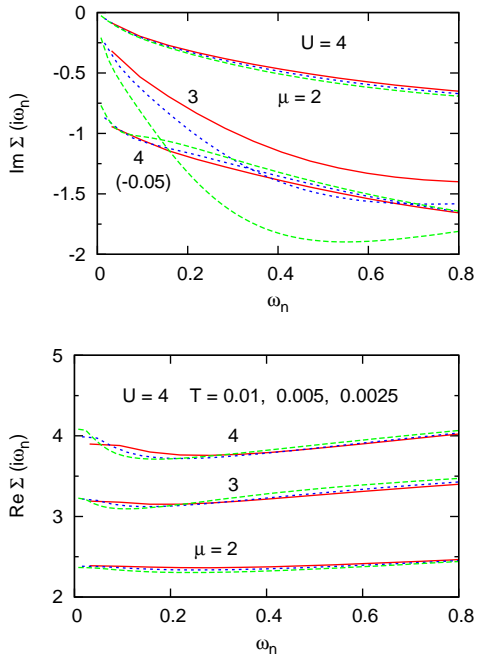


FIG. 6: (Color online) Low-energy region of self-energy of three-band model for several chemical potentials at temperatures $T = 0.01$ (red solid curves), $T = 0.005$ (short-dashed blue curves), and $T = 0.0025$ (long-dashed green curves); $U = 4$, $J = U/6$, $n_s = 9$ (two bath levels per impurity orbital). For clarity, the curves in the upper panel for $\mu = 4$ are shifted down by 0.05.

$G_{0,m}^{cl}(i\omega_n)$, Eq. (6). These functions are compared in Figure 5 for several chemical potentials, assuming two bath levels per orbital. Evidently, at $T = 0.01$, the fit of the bath Green's function with 5 parameters is already remarkably good. Including more bath levels improves the fit at low ω_n even further. Also shown is the discretization of $G_{0,m}$ at $T = 0.0025$ for $\mu = 2$. In this case the fit is much less satisfactory, indicating that more bath levels are required at this low temperature.

The results in Figure 5 are based on minimization of $|G_0 - G_0^{cl}|$ as in Eq. (22), using the weight function $W_n = 1/\omega_n^N$, where $N = 1$. In Appendix A.1 it is shown that discretizations of similarly good quality are obtained for $N = 0$ and $N = 2$, as well as for minimization of $|1/G_0 - 1/G_0^{cl}|$, as in Eq. (23), with $N = 0, 1, 2$.

It should be noted that the small kinks in $\text{Im } G_{0,m}^{cl}(i\omega_n)$ at low ω_n are related to the fact that, because of the finite size of the cluster, the cluster spectrum is always gapped. Thus, $\text{Im } G_{0,m}^{cl}(i\omega) = 0$ in the limit $\omega \rightarrow 0$, giving rise to large deviations from the lattice bath Green's function (see also Section 3.5 and Figure 21). These deviations occur primarily at very low frequencies near or below ω_0 . Naturally, they are much less pronounced if the system is insulating. To achieve an accurate discretization of $G_{0,m}$ with a small number of bath levels it is there-

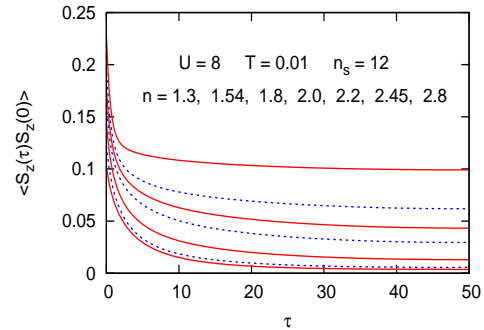


FIG. 7: (Color online) Spin-spin correlation function for degenerate three-band model at various occupancies (increasing from below) for $n_s = 12$; $U = 4$, $J = U/6$, $T = 0.01$. In the Fermi-liquid regime at small n , the susceptibility is Pauli-like, whereas at larger n it reflects Curie-Weiss behavior.

fore necessary to use a Matsubara grid for not too low temperatures. On the basis of the example shown in Figure 5 and various other systems involving multi-orbital and multi-site correlations, $T \approx 0.005, \dots, 0.01$ is a reasonable lower limit, if two or three bath levels per orbital are available.

Although the discretization of the bath Green's function becomes less accurate at low temperatures, the self-consistently determined self-energy can still be qualitatively correct. To illustrate this point, we show in Figure 6 the self-energy at $T = 0.01, 0.005$, and 0.0025 . Evidently, all curves exhibit the same trend as a function of chemical potential, with Fermi-liquid behavior at low occupancy ($\mu = 2$, $n \approx 1.6$) and a pronounced low-energy scattering rate closer to half-filling ($\mu = 4$, $n \approx 2.5$). As in Figure 4, the results near the spin freezing phase boundary ($\mu = 3$, $n \approx 2$) are most sensitive and therefore show larger variation with T .

As shown in Ref. [47], the physical reason for the change of the self-energy from Fermi-liquid to non-Fermi-liquid behavior seen in Figure 3 is associated with a qualitative change of the spin-spin correlation function $C_m(\tau) = \langle S_{mz}(\tau)S_{mz}(0) \rangle$, where τ denotes imaginary time. In the Fermi-liquid regime $\mu < 3$, this function decays with τ , so that $C_m(\tau = \beta/2)$ is very small. The susceptibility $\chi_m \sim \int_0^\beta d\tau \langle S_{mz}(\tau)S_{mz}(0) \rangle$ then is Pauli-like, i.e., independent of temperature. For $\mu > 3$, however, $C_m(\tau)$ approaches a finite value for $\tau \rightarrow \beta/2$, so that χ_m becomes proportional to $1/T$, as expected for Curie-Weiss behavior due to the formation of local moments. Figure 7 shows the correlation function as calculated within ED DMFT. The variation of $C_m(\tau)$ with doping found here agrees rather well with the continuous-time QMC results discussed in Ref. [47].

We note here that a similar sequence of phases, from a Mott insulator at half-filling towards non-Fermi-liquid and Fermi-liquid behavior with increasing electron or

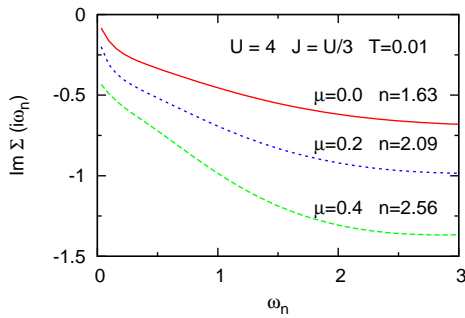


FIG. 8: (Color online) Imaginary part of self-energy of three-band model at $U = 4$, $J = U/3$ for several chemical potentials. $T = 0.01$, $n_s = 12$. Note the onset and low-energy kink.

hole doping, is also seen in the five-band Hubbard model discussed in Section 3.3 and in the non-local properties of the single-band Hubbard model discussed in Section 3.5.

Apart from the spin freezing transition, the three-band model exhibits another interesting phenomenon not present in the single-band case. As shown in Figure 8, for Hund exchange $J = U/3$ at $U = 4$, the imaginary part of the self-energy reveals not only a finite low-energy scattering rate, but also a kink at about $\omega_n \approx 0.2$. Extrapolation of the self-energy to real ω yields a resonance in $\text{Im} \Sigma(\omega)$ near $\omega = -0.2$ (below $E_F = 0$), which is weak in the Fermi-liquid region ($n < 2$), but gets very pronounced in the non-Fermi-liquid range ($n > 2$). Moreover, the resonance disappears at small J . The reason for this dependency on J is the fact that, at half-filling, the three-band Hubbard model is metallic at small J , and becomes Mott insulating for sufficiently large J [48, 49]. Thus the resonance exists only in proximity to the Mott phase in the limit of half-filling. It can also be shown that the peak in $\text{Im} \Sigma(\omega)$ gives rise to a pseudogap in the density of states slightly below E_F and that it is associated with a maximum in the local spin correlation function. The resonance in the self-energy induced via Hund coupling may therefore be viewed as a collective mode caused by spin fluctuations. According to Figure 8, the non-Fermi-liquid behavior associated with the low-energy onset of $\text{Im} \Sigma(\omega)$ can then be interpreted as a consequence of the appearance of this collective mode. A similar phenomenon occurs in the five-band Hubbard model discussed in Section 3.3. For a discussion of collective modes due to spin fluctuations in the single-band Hubbard model, see Ref. [50].

3.2. Three-Band Materials

The multi-band ED DMFT approach outlined in Section 2.1 has recently been used to study the role of local

Coulomb interactions in several materials with partially filled t_{2g} bands, where the e_g subbands are pushed above the Fermi level as a result of crystal field effects. In this subsection, we summarize the main results of these calculations, illustrate the convergence of the self-energy with the size of the bath, and point out the consistency with complementary QMC DMFT results.

3.2.1. $\text{Ca}_{2-x}\text{Sr}_x\text{RuO}_4$

A system that has been studied extensively is the layer perovskite $\text{Ca}_{2-x}\text{Sr}_x\text{RuO}_4$ which exhibits a remarkably rich phase diagram, ranging from unconventional superconductivity in the pure Sr limit to an antiferromagnetic Mott insulator at $x = 0$, with a variety of exotic magnetic phases at intermediate concentrations [51]. As the substitution of Sr by the slightly smaller Ca ions is isoelectronic at occupancy $4d^4$, the various electronic and magnetic phases are entirely the result of subtle hybridization changes among the t_{2g} states caused by structural distortions. Because of the essentially two-dimensional structure of this material, the d_{xy} band has a much larger band width than the more nearly one-dimensional $d_{xz,yz}$ bands. Thus, Coulomb interactions can be expected to modify these subbands differently. Moreover, LDA calculations [52] predict the d_{xy} van Hove singularity for $x = 2$ to lie only about 50 meV above the Fermi level, so that correlation induced charge transfer between the t_{2g} bands could possibly shift this singularity below E_F , giving rise to a qualitative change of the topology of the d_{xy} Fermi surface from electron-like to hole-like. Multi-band QMC and ED DMFT calculations for Sr_2RuO_4 do indeed predict a decrease of orbital polarization, i.e., a shift of charge from $d_{xz,yz}$ to d_{xy} [53–57]. The concomitant lowering of the d_{xy} van Hove singularity for realistic interaction parameters, however, is not large enough to modify the topology of the Fermi surface.

The upper panel of Figure 9 illustrates the convergence of the ED self-energy components with cluster size for a tight-binding Hamiltonian including up to second-neighbor hopping interactions [53]. The results are for full Hund exchange and the values of U and J correspond to those derived in recent constrained RPA calculations [57]. There is good agreement for two and three bath levels per impurity orbital, especially at low energies. The small differences are mainly caused by slightly different orbital occupancies obtained for these two bath sizes. For $n_s = 12$, we find $n_{xy} = 0.66$ and $n_{xz,yz} = 0.67$. The uncorrelated subband occupancies are $n_{xy} = 0.63$ and $n_{xz,yz} = 0.68$. Thus, Coulomb correlations in the pure Sr compound lead to decreasing orbital polarization. The effective mass enhancement is approximately $m^*/m_{\text{LDA}} \approx 4$, in agreement with continuous-time QMC calculations [57] and with experiment [51]. In this sense, it is appropriate to regard Sr_2RuO_4 as a strongly correlated material.

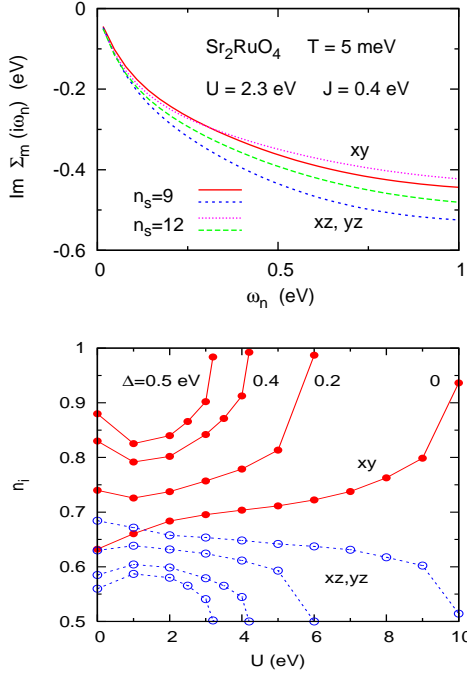


FIG. 9: (Color online) Upper panel: Imaginary part of Sr_2RuO_4 t_{2g} self-energy components for cluster sizes $n_s = 9$ and $n_s = 12$; $U = 2.3$ eV, $J = 0.4$ eV, $T = 5$ meV. Lower panel: Orbital occupancies (per spin) of $\text{Ca}_{2-x}\text{Sr}_x\text{RuO}_4$ t_{2g} subbands as functions of Coulomb energy for various crystal field splittings Δ , derived within ED DMFT ($n_s = 9$) [56]. Solid (red) dots: n_{xy} , empty (blue) dots: $n_{xz,yz}$. Hund exchange $J = U/4$; $T = 20$ meV.

For a tight-binding model similar to the one used in Ref. [53], continuous-time QMC results [58] for the self-energy agree very well with those in Figure 9. In particular, they show little difference between the d_{xy} and $d_{xz,yz}$ effective mass enhancements. Stronger t_{2g} anisotropy is obtained for a more accurate single-particle Hamiltonian, for which the d_{xy} van Hove singularity lies closer to E_F and the difference in d_{xy} and $d_{xz,yz}$ band widths is less pronounced than in the tight-binding model [57].

Substitution of Sr via Ca leads to rotation, tilting and flattening of Oxygen octahedra and, as a result, to a lowering of the d_{xy} band with respect to the $d_{xz,yz}$ bands [59, 60]. To investigate the influence of Coulomb correlations in the presence of this structurally induced interorbital charge transfer we have performed ED DMFT calculations, with an additional crystal field $\Delta = \epsilon_{xz,yz} - \epsilon_{xy}$ to account for the downward shift of the d_{xy} bands [56]. As shown in the lower panel of Figure 9, correlations greatly enhance the $d_{xz,yz} \rightarrow d_{xy}$ charge transfer (except at small values of U). In fact, for realistic values of Δ , U , and J , the d_{xy} band gets completely filled and the half-filled $d_{xz,yz}$ bands become Mott insulating. This orbital polarization is also evident in the cluster spectra which are depicted in Figure 10 for $\Delta = 0.4$ eV. At $U = 3.0$ eV, the

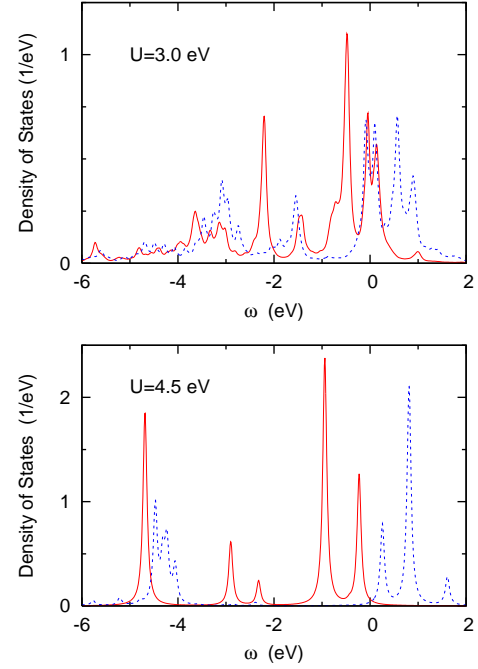


FIG. 10: (Color online) Quasiparticle spectra of Ca_2RuO_4 for crystal-field splitting $\Delta = 0.4$ eV at $U = 3.0$ eV (upper panel) and $U = 4.5$ eV (lower panel) for $J = U/4$, $T = 20$ meV. Solid (red) curves: d_{xy} band, dashed (blue) curves: $d_{xz,yz}$ bands. The spectra are derived from the interacting cluster Green's function for $n_s = 9$, with broadening $\gamma = 50$ meV [56].

system is metallic, and all three t_{2g} orbitals contribute to the density of states at E_F . At $U = 4.5$ eV, however, the d_{xy} band is pushed below E_F and the doubly degenerate $d_{xz,yz}$ bands are split into lower and upper Hubbard bands. Within the accuracy of the ED DMFT calculations, the filling and Mott-splitting of subbands takes place at the same critical $U_c \approx 4.2$ eV. Thus, there are no orbital-selective, successive Mott transitions for the narrow $d_{xz,yz}$ and wide d_{xy} subbands, in contrast to the mechanism proposed by Anisimov *et al.* [54]. Recent continuous-time QMC DMFT results for Ca_2RuO_4 by Gorelov *et al.* [60] based on detailed LDA calculations also do not find successive transitions. Orbital selective Mott phases can appear, however, if the t_{2g} crystal field splitting is assumed to have the opposite sign [61].

We point out that the large critical Coulomb energies seen in the lower panel of Figure 9 for small values of Δ are a consequence of the assumption $J = U/4$. If J is held fixed at a realistic value, U_c becomes accordingly smaller. For $U = 3.1$ eV and $J = 0.7$ eV, as in Ref. [60], we have $J \approx U/4$ so that the orbital polarization obtained for $\Delta \approx 0.4, \dots, 0.5$ eV is qualitatively correct.

3.2.2. LaTiO_3

The nature of the Mott transition in Ca_2RuO_4 , where

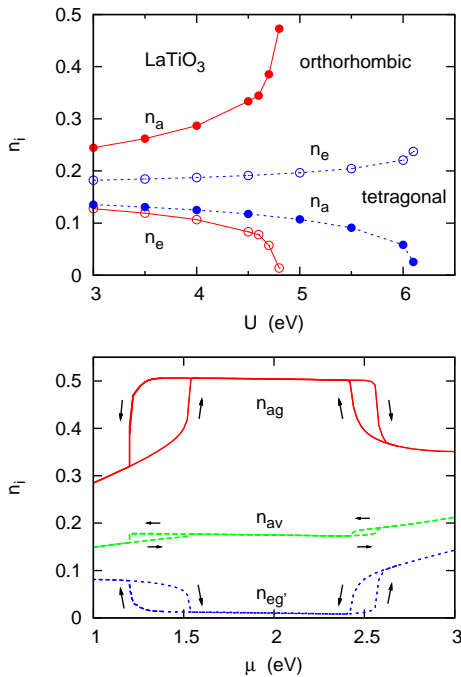


FIG. 11: (Color online) Upper panel: LaTiO₃ subband occupancies for orthorhombic and tetragonal bulk geometry. Since the crystal field splitting has the opposite sign in these structures, the orbital polarization between the singly degenerate a_g (d_{xy}) and doubly degenerate $e_{g'}$ ($d_{xz,yz}$) states is reversed [63]. Lower panel: LaTiO₃ t_{2g} subband occupancies per spin as functions of chemical potential. $U = 5$ eV, Hund exchange $J = 0.65$ eV, $T = 20$ meV. Also shown is the average occupancy $n_{av} = (n_{ag} + 2n_{eg'})/3$. The arrows indicate the hysteresis for increasing and decreasing μ [66].

the correlation induced crystal field enhancement leads to strong orbital polarization, is similar to the one discussed by Pavarini *et al.* [62] for LaTiO₃ ($3d^1$). In contrast to cubic SrVO₃, the orthorhombic structure of LaTiO₃ gives rise to a splitting of about 0.2 eV between the singly degenerate a_g and doubly degenerate $e_{g'}$ states, implying appreciably different subband occupancies: $n_{a_g} \approx 0.23$ and $n_{e_{g'}} \approx 0.135$ per spin. This orbital polarization is strongly enhanced by the local Coulomb interaction, leading to virtually empty $e_{g'}$ subbands and a Mott phase in the half-filled a_g band. Finite-temperature ED DMFT results [63] which are shown in upper panel of Figure 11 are consistent with this picture.

Interestingly, when thin layers of LaTiO₃ are deposited on cubic SrTiO₃, as in LaTiO₃/SrTiO₃ heterostructures, the initial growth appears to be tetragonal [64]. This substrate-enforced reconstruction gives rise to an increased t_{2g} band width and to a reversal of the t_{2g} crystal field. As also shown in the upper panel of Figure 11, the result of these effects is an increase of the critical Coulomb energy for the Mott transition, and qualitatively different subband occupancies. Now the

singly-degenerate d_{xy} band is emptied, and the quarter-filled $d_{xz,yz}$ bands are split into lower and upper Hubbard bands. These results are relevant for the interpretation of the metallicity observed LaTiO₃/SrTiO₃ heterostructures [65]. If realistic values of U for LaTiO₃ are about 5.0, ..., 5.5 eV, the results in Figure 11 imply that thin LaTiO₃ layers are strongly correlated metals rather than Mott insulators. Thus, the experimentally observed metallic behavior is not associated with the atomic interface Ti layers with nominal $3d^{0.5}$ occupancy, but with the entire LaTiO₃ slabs.

The lower panel of Figure 11 demonstrates that the t_{2g} orbital polarization is also highly sensitive to electron and hole doping [66]. Since the subband compressibilities $\kappa_m = \partial n_m / \partial \mu$ diverge at the Mott transition, small changes away from the nominal $n = 1$ occupancy cause significantly larger changes in subband occupancies. In fact, weak overall hole doping gives rise to much larger hole doping in the half-filled a_g band, accompanied by electron doping in the $e_{g'}$ bands. Conversely, weak overall electron doping of the system gives rise to much larger electron doping in the empty $e_{g'}$ bands, accompanied by hole doping of the a_g band. Thus, near the Mott transition, pronounced internal charge rearrangement takes place among the relevant subbands.

ED DMFT cluster spectra illustrating the doping dependence in LaTiO₃, and cluster spectra corresponding to the orthorhombic and tetragonal bulk phases, can be found in Refs. [66] and [63], respectively.

3.2.3. V₂O₃

Another material that exhibits enhanced orbital polarization near the Mott transition is V₂O₃ ($3d^2$) [67]. In this case, the corundum lattice geometry ensures that the doubly-degenerate $e_{g'}$ bands have a slightly larger binding energy than the singly-degenerate a_g band. In Ref. [40], we have used ED DMFT to analyze this orbital polarization for $n_s = 9$, i.e., using two bath levels per impurity orbital. Figure 12 illustrates the quality of the discretization of the bath Green's function $G_{0,m}(i\omega_n)$ components. As pointed out above, cluster spectra are always gapped, so that $\text{Im} G_{0,m}^{cl}(i\omega_n) \rightarrow 0$ at very low frequencies. This limiting behavior is discernible, however, only below $\omega_0 = \pi T = 0.031$ eV, where the lattice and cluster Green's functions strongly deviate from one another. Thus, by choosing a Matsubara grid with a temperature not much lower than $T \approx 10$ meV, these discrepancies are almost completely avoided and the finite cluster can serve as an adequate representation of the lattice continuum.

Figure 13 shows the Coulomb driven enhancement of the V₂O₃ orbital polarization. Near $U \approx 5$ eV, the a_g band is pushed above the Fermi level and the half-filled $e_{g'}$ bands are split into lower and upper Hubbard peaks. Note that the precise value of the critical Coulomb

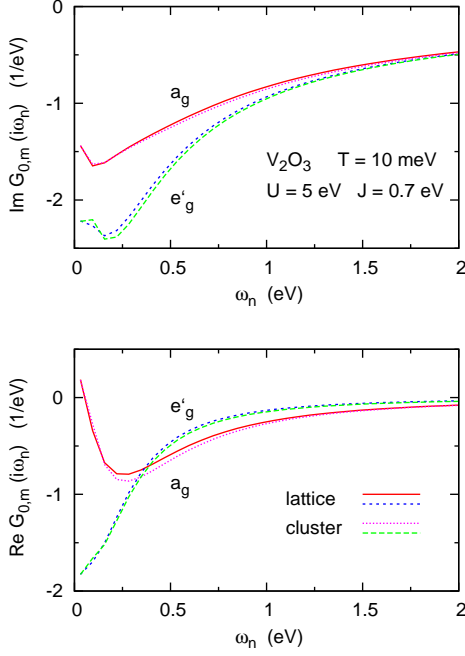


FIG. 12: (Color online) Discretization of V_2O_3 bath Green's function components, using two bath levels per impurity orbital; $U = 5$ eV, $J = 0.7$, $T = 10$ meV. Upper (lower) panel: imaginary (real) part.

energy depends sensitively on the exchange terms included among the many-body interactions. In the case of only density-density terms (Ising-like exchange), we find $U_c \approx 5.1$ eV, in agreement with Hirsch-Fye QMC DMFT calculations by Keller *et al.* [67]. Full Hund exchange, on the other hand, shifts U_c upward to about 5.6 eV, a trend that is consistent with results obtained in ED and NRG studies of simpler two-band models [19, 68].

The lower panel of Figure 13 shows the convergence of the self-energy components in the metallic phase close to the Mott transition with bath size. The nearly half-filled $e_{g'}$ subbands are seen to exhibit a significant low-energy scattering rate which is reminiscent of the spin freezing transition in the degenerate three-band model discussed in Section 3.1. The nearly empty a_g band, on the other hand, is much more itinerant. Nevertheless, it exhibits a large effective mass enhancement of about 5, and a small but finite scattering rate caused by the interaction with the almost Mott-localized $e_{g'}$ states. The differences for $n_s = 9$ and $n_s = 12$ are presumably caused by slightly different orbital occupancies. Close to a transition, the self-energy is particularly sensitive to small parameter changes. A similar effect was found close to the spin-freezing transition in the degenerate three-band model discussed in Section 3.1.

3.2.4. $Na_{0.3}CoO_2$

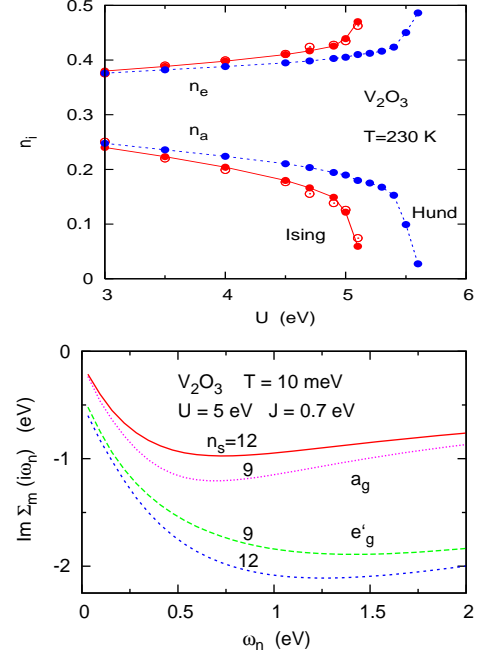


FIG. 13: (Color online) Upper panel: V_2O_3 subband occupancies per spin as functions of Coulomb energy. Red symbols: Ising exchange, blue symbols: full Hund exchange. Solid dots: ED DMFT [40], empty dots: QMC DMFT [67]. Lower panel: imaginary part of self-energy components for two and three bath levels per impurity orbital ($n_s = 9$ and $n_s = 12$, respectively) at $U = 5$ eV, $J = 0.7$, $T = 10$ meV.

Despite several years of experimental and theoretical investigations, basic features of the electronic properties of the intercalated layer compound Na_xCoO_2 are still controversial. The doping concentration $x = 0.3$ is of particular interest since this material becomes superconducting when small amounts of water are added [69].

As a result of the octahedral crystal field, the Co $3d$ bands are split into t_{2g} and e_g subbands. With Na doping the occupancy of the t_{2g} sector can be continuously tuned between $n = 5$ and $n = 6$. The rhombohedral symmetry at Co sites yields a further splitting of t_{2g} orbitals into singly-degenerate a_g and doubly-degenerate $e_{g'}$ states. Because of the nearly two-dimensional hexagonal structure, the Fermi surface as predicted by LDA calculations [70] exhibits a large a_g hole pocket centered at Γ , and six small $e_{g'}$ hole pockets along the ΓK directions of the Brillouin Zone. These small pockets have so far not been observed in ARPES measurements [71, 72]. As discussed above, local Coulomb interactions can give rise to charge transfer between subbands, implying increasing or decreasing orbital polarization, depending on the details of the single-particle Hamiltonian. Several groups have carried out DMFT calculations in order to explore whether the small pockets might disappear be-

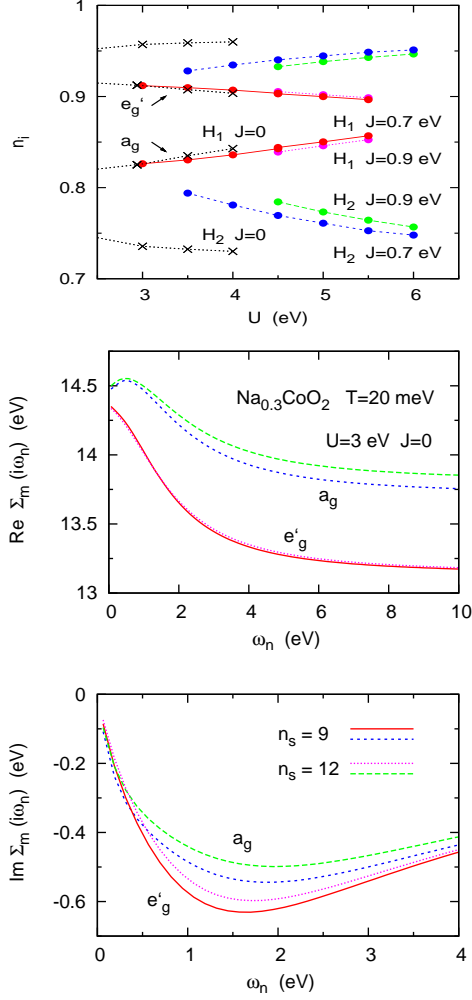


FIG. 14: (Color online) Upper panel: $\text{Na}_{0.3}\text{CoO}_2$ subband occupancies as functions of Coulomb energy for two single-particle Hamiltonians H_1 and H_2 (see text) and different Hund exchange energies J [74]. Lower two panels: Real and imaginary components of $\text{Na}_{0.3}\text{CoO}_2$ self-energy calculated within ED DMFT for two and three bath levels per impurity t_{2g} orbital; Hamiltonian H_2 , $U = 3$ eV, $J = 0$, and $T = 20$ meV.

cause of a_g to $e_{g'}$ electron transfer [20, 73–76].

The upper panel of Figure 14 summarizes the degree of orbital polarization obtained for slightly different single-particle Hamiltonians H_1 and H_2 , as well as different Hund couplings J [74]. The important difference between these Hamiltonians is that, because of different band crossings in the tight-binding fits, the effective crystal field $\Delta = \epsilon_{a_g} - \epsilon_{e_{g'}}$ is about -130 meV for H_1 , while it is -10 meV for H_2 . The band crossings obtained for H_1 correspond to those of high-quality LAPW LDA calculations. As shown in the figure, these two tight-binding fits yield opposite trends of the orbital occupancy with increasing local Coulomb energy. H_1 gives rise to de-

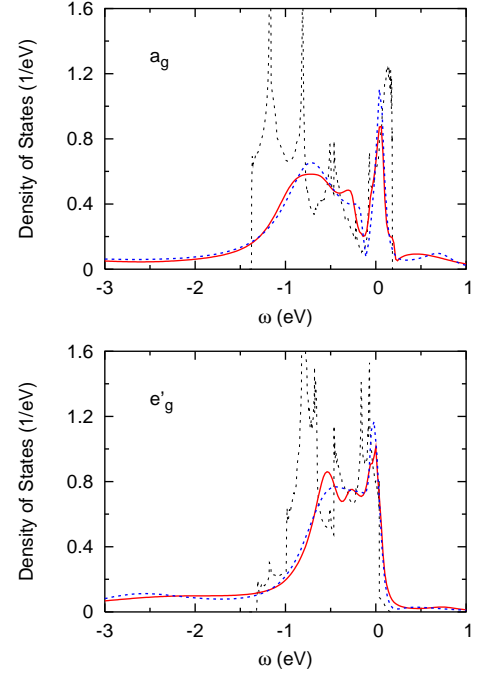


FIG. 15: (Color online) Quasiparticle spectra for a_g (upper panel) and $e'_{g'}$ (lower panel) subbands of $\text{Na}_{0.3}\text{CoO}_2$ at $U = 3$ eV, $J = 0.75$ eV, $T = 10$ meV. Solid (red) curves: spectra derived from lattice Green's function $G_m(\omega)$ after extrapolation of $\Sigma_m(i\omega_n)$ to real ω ; dashed (blue) curves: spectra derived via extrapolation of $G_m(i\omega_n)$; dotted (black) curves: single-particle density of states [20].

creasing orbital polarization, whereas H_2 leads to increasing orbital polarization. These different trends are maintained even if the Coulomb and energies are varied over wide ranges, $U \approx 3, \dots, 6$ eV and $J = 0, \dots, 0.9$ eV. Evidently, correlation effects are not strong enough to fill the $e_{g'}$ pockets.

The lower panels of Figure 14 illustrate the convergence of the ED self-energy components of Na_xCoO_2 with cluster size, using Hamiltonian H_2 . The small differences obtained for $n_s = 9$ and $n_s = 12$ are partly related to the slightly different occupancies: $n_{a_g} = 0.753$ (0.740) and $n_{e'_{g'}} = 0.946$ (0.959) for $n_s = 9$ ($n_s = 12$). The important low-frequency features are seen to be in very good agreement for these cluster sizes, in particular, the small upward shift of a_g states relative to $e_{g'}$ by about 0.15 eV. We also point out that these ED results for H_2 are fully consistent with the ones obtained within QMC for the same Hamiltonian [76]. In fact, the detailed comparison of the respective self-energy components shows, that, if identical input parameters are employed, nearly quantitative agreement is found for these impurity solvers [77].

The $e_{g'}$ pockets can be made to vanish by adjusting the t_{2g} crystal field to $\Delta = 40, \dots, 90$ meV [76]. As a result, the $e_{g'}$ bands are pushed down, and Coulomb correlations can fill them completely. The physical origin of such a

modification of the crystal field is presently unknown. A possible source of the discrepancy between theory and experiment is that ARPES is surface sensitive. As shown by Pillay *et al.* [78], the surface layer of Na ions can give rise to an effective t_{2g} crystal field, which substantially lowers the e_g' bands with respect to the a_g bands.

The results shown in Figure 14 underline the complex interplay between kinetic energy and Coulomb repulsion in strongly correlated materials. While in some systems, such as LaTiO_3 and V_2O_3 , orbital polarization tends to be enhanced by onsite Coulomb interactions, other systems, such as $\text{Ca}_{2-x}\text{Sr}_x\text{RuO}_4$ and Na_xCoO_2 , exhibit more complex patterns. Because of their two-dimensional geometry, these oxides comprise subbands of very different widths and spectral shapes. Orbital fluctuations can then be enhanced or reduced as a result of Coulomb correlations.

As pointed out before, quasi-particle spectra at real ω can be derived by analytic continuation of the lattice Green's function $G_m(i\omega_n)$, or by first extrapolating $\Sigma_m(i\omega_n)$ to real ω and then evaluating $G_m(\omega)$. The comparison shown in Figure 15 demonstrates that both methods are consistent. Nonetheless, the latter method is seen to retain finer spectral details originating from the single-particle Hamiltonian. For instance, the e_g spectrum shows two peaks below E_F which evidently are the shifted and broadened density of states features near 0.4 eV and 0.8 eV below the Fermi level. Also, the peak close to E_F exhibits some of the fine structure of the single-particle density of states. These details are lost if the spectrum is instead derived via analytic continuation of the lattice Green's function.

3.3. Degenerate Five-Band Model

The discovery of superconductivity in iron pnictides and chalcogenides has stimulated a variety of investigations concerning the role of Coulomb correlations in these materials. In contrast to high- T_c cuprates, which have antiferromagnetic Mott insulators as parent compounds, pnictides are correlated magnetic metals showing significant deviations from Fermi-liquid behavior. Moreover, as a result of the multi-band nature of pnictides, the interplay of Coulomb and exchange interactions give rise to phenomena not found in cuprates.

As there is no clear distinction between t_{2g} and e_g subbands in compounds such as FeAsLaO and FeSe , we have recently extended ED DMFT to five bands, where each of the impurity orbitals hybridizes with two bath levels ($n_s = 15$) [34]. Because of the enormous size of the resulting Hilbert space, the cluster Green's function is evaluated at $T = 0$, i.e., for $\beta \rightarrow \infty$ in Eq. (8), while the Matsubara grid corresponds to $T \approx 0.01$.

The main result of this study is the identification of a spin freezing transition near the nominal $n = 6$ occu-

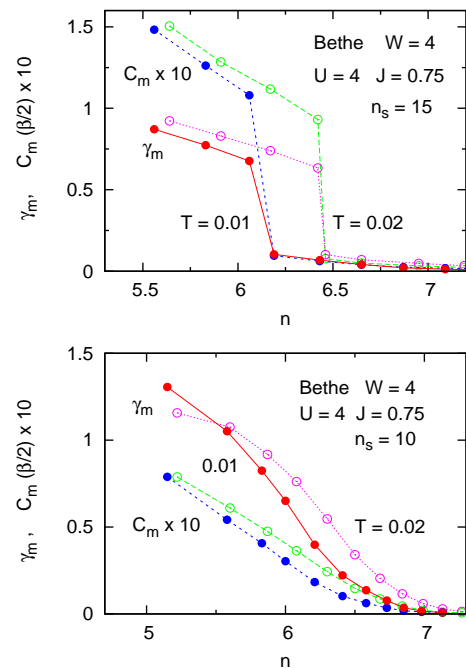


FIG. 16: (Color online) Low-energy scattering rates and spin-spin correlations derived within ED DMFT for a degenerate five-band model with Bethe lattice density of states ($W = 4$); $U = 4$, $J = 0.75$. Solid dots: $T = 0.01$, empty dots: $T = 0.02$. Upper panel: $n_s = 15$; lower panel $n_s = 10$.

pancy of the Fe $3d$ states, i.e., approximately one electron away from the Mott phase at half-filling. Towards larger occupancies (electron doping), ordinary Fermi liquid behavior is restored, whereas occupancies lower than $n \approx 6$ (hole doping) give rise to more pronounced non-Fermi-liquid-like deviations caused by a non-vanishing scattering rate. Accordingly, the spin-spin correlation function $C_m(\tau) = \langle S_{mz}(\tau)S_{mz}(0) \rangle$ changes from Pauli-like at large doping to Curie-Weiss-like at smaller doping. These findings are closely related to the spin-freezing transition [47] in the degenerate three-band model near $n = 2$ occupancy, i.e., about one electron away from the Mott phase at half-filling (see Section 3.1).

Making use of an accurate single-particle Hamiltonian $t(\mathbf{k})$, derived from maximally localized Wannier functions, and constrained RPA interaction parameters calculated within the same basis [79], it was also shown that, because of larger Coulomb interactions, FeSe lies on the non-Fermi-liquid side of the spin freezing transition, while FeAsLaO corresponds to a moderately correlated Fermi liquid [80]. Deviations from Fermi-liquid behavior were recently also shown to occur in the paramagnetic phase of $\alpha\text{-Fe}$ [81].

To elucidate the extent to which these results are related to crystal field effects and orbital polarization, we consider a fully degenerate five-band model, with semi-

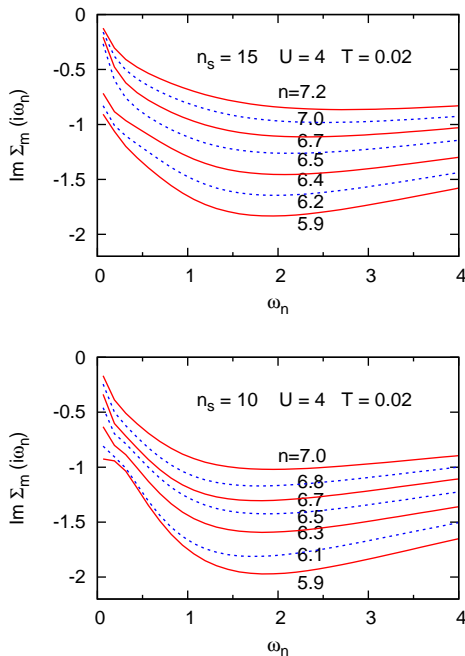


FIG. 17: (Color online) Self-energy of degenerate five-band model for several occupancies near the spin freezing transition; $U = 4$, $T = 0.02$. Upper panel: $n_s = 15$, two bath levels per impurity orbital. Lower panel: $n_s = 10$, one bath level per impurity orbital. Note the onsets and low-energy kinks.

elliptical density of states components of width $W = 4$ ($W = 4$ eV corresponds to typical pnictide compounds). Using interaction parameters similar to those in FeSe, we find a spin-freezing transition at about $n = 6.2$ occupancy, implying non-Fermi-liquid properties for $n = 6$. The upper panel of Figure 16 shows the variation of the low-energy scattering rate, $\gamma_m = |\text{Im} \Sigma_m(i\omega_n \rightarrow 0)|$, with band occupancy for $T = 0.01$ and $T = 0.02$, assuming two bath levels per impurity orbital. Both Matsubara grids indicate a Fermi-liquid to non-Fermi-liquid transition near $n = 6.2, \dots, 6.4$. The spin correlation function $C_m(\beta/2)$ changes from Pauli to Curie-Weiss behavior in the same occupancy range.

Because of the importance of strongly correlated five-band transition metals and transition metal oxides, it is of great interest to investigate whether ED DMFT calculations with only one bath level per impurity orbital can provide useful qualitative information concerning crucial dynamical properties of the system. Calculations for $n_s = 10$ (the dimension of largest sector of the Hilbert space is $N = 63504$) are extremely fast, requiring only few minutes per iteration at typical temperatures. Thus, for a qualitative exploration of the phase diagram they would be highly valuable, before more accurate but time-consuming calculations for $n_s = 15$ are carried out.

The lower panel of Figure 16 shows the scattering rate

and spin correlation function as functions of band occupancy for $n_s = 10$, i.e., for only one bath level per impurity orbital. Both quantities now exhibit a less abrupt change from Fermi-liquid behavior at large n to non-Fermi-liquid behavior at small n than for $n_s = 15$. Nevertheless, qualitatively, these results also suggest the existence of a spin-freezing transition near $n = 6.5$ occupancy. Evidently, this transition is not caused by orbital polarization. As in the case of the three-band model [47], it is purely related to many-electron Coulomb and exchange interactions at about one electron away from half-filling.

Figure 17 illustrates the influence of the bath size on the self-energy. While uncertainties at low frequencies are larger for $n_s = 10$ than for $n_s = 15$, the qualitative picture is the same in both cases. At large occupancies, $\text{Im} \Sigma_m(i\omega_n) \sim \omega_n$ for $\omega_n \rightarrow 0$, consistent with Fermi-liquid properties. At about $n \approx 6.5$, $\text{Im} \Sigma_m$ begins to exhibit an onset, indicating the breakdown of Fermi-liquid behavior due to the presence of frozen moments. It would be very interesting to compare the ED results shown in Figs. 16 and 17 with corresponding data obtained via continuous-time QMC DMFT.

The overall consistency of the five-band results for $n_s = 10$ with the more accurate ones for $n_s = 15$ might be very useful for future applications involving five-band materials. The computationally rather straightforward ED DMFT approach for $n_s = 10$ could then be used to scan a wide range of system parameters, such as temperature, pressure (band width), crystal field splitting, doping concentration, Coulomb and exchange interactions, etc. For greater accuracy, more demanding calculations with $n_s = 15$ could then be performed near critical values of some of these parameters. One could also consider extending finite-temperature ED DMFT to f -electron systems with $n_c = 7$ orbitals, using 7 bath levels, i.e. $n_s = 14$.

We close this subsection by pointing out that the self-energies shown in Figure 17 do not only exhibit a low-energy onset towards half-filling, but also a kink near $\omega_n \approx 0.1$ eV. Extrapolation of $\Sigma_m(i\omega_n)$ to real ω reveals that this kink is associated with a resonance in $\text{Im} \Sigma_m(\omega)$ which gives rise to a pseudogap in the density of states slightly above the Fermi level. In fact, the non-vanishing low-energy scattering rate may be viewed as a result of this resonance in the self-energy. As shown in Ref. [82], the pseudogap is remarkably stable over a wide range of Coulomb and exchange energies, as long as J is not too small. The upper panel of Figure 18 illustrates some of these quasi-particle spectra, which are derived by analytic continuation of the lattice Green's function. Moreover, the local spin correlation function exhibits a pronounced maximum at low energies, suggesting that the peak in the self-energy corresponds to a collective mode induced by spin fluctuations. These features disappear at small J (see the spectrum for $U = 3$ eV, $J = 0$). This be-

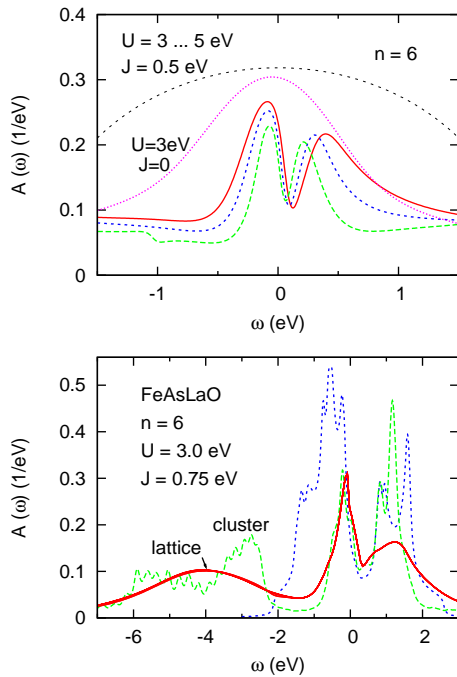


FIG. 18: (Color online) Upper panel: Low-energy region of spectral distribution of degenerate five-band model ($W = 4$ eV) at occupancy $n = 6$, calculated within ED DMFT ($n_s = 10$) for several Coulomb energies: $U = 3$ eV (solid red curve), $U = 4$ eV (short-dashed blue curve), and $U = 5$ eV (long-dashed green curve); $J = 0.5$ eV. Spectra for $J = 0.75$ eV and $J = 1$ eV are similar. Also shown is the result for $U = 3$ eV, $J = 0$ (dotted magenta curve). The bare density of states is indicated by the black dashed curve. Lower panel: Fe 3d quasiparticle spectra of FeAsLaO, calculated within ED DMFT ($n_s = 15$) for $U = 3$ eV, $J = 0.75$ eV [82]. Solid (red) curve: lattice spectrum; long-dashed (green) curve: cluster spectrum. The bare 3d density of states is indicated by the short-dashed blue curve [79].

behavior is intimately related to the fact that, at half-filling, the system is a Mott insulator for $J = 0.5, \dots, 1.0$ eV, while it becomes metallic for small J . Thus, the Mott phase in this multi-band system, and the collective mode in $\text{Im}\Sigma_m(\omega)$ away from half-filling, are a consequence of Hund coupling. Qualitatively similar behavior is also found in the degenerate three-band Hubbard model discussed in Section 3.1.

The pseudogap induced via Hund coupling found in the degenerate five-band model might be relevant also for the understanding of the electronic properties of iron-based pnictides. As shown in Figure 18 (lower panel) for FeAsLaO, the bare density of states as well as the quasiparticle spectrum (obtained via analytic continuation of the lattice Green's function) reveal a pronounced minimum slightly above E_F . (Also shown is the corresponding cluster spectrum, which agrees well with the lattice spectrum in the vicinity of E_F .) Similar features have been obtained for a variety of pnictides (see, for instance,

Ref. [83]). The results for the degenerate five-band suggest that the pseudogap above E_F is a generic feature caused by multi-band Coulomb correlations within the 3d shell and that its existence depends crucially on realistic values of Hund coupling. The paramagnetic quasiparticle distribution of actual pnictides should therefore consist of a combination of correlation features associated with J and signatures related to the bare density of states. Evidence for this behavior seems to have been observed in recent experimental optical data for BaFe₂Se₂ [84, 85].

3.4. Triangular Lattice

The role of spatial fluctuations is of great importance for a variety of strongly correlated systems, in particular, in the high- T_c cuprates, in organic crystals, and in graphene. In the next three subsections we use the cluster extension of finite-temperature ED DMFT to elucidate the non-local properties of the self-energy for various two-dimensional single-band materials.

The layered charge transfer salts κ -(BEDT-TTF)₂X, where X denotes inorganic monovalent anions such as Cu[N(CN)₂]Cl or Cu₂(CN)₃, exhibit a remarkably rich series of phases as function of hydrostatic pressure, including Fermi-liquid and bad-metallic behavior, superconductivity, as well as paramagnetic and antiferromagnetic insulating phases [86, 87]. Since these compounds have triangular lattice geometries, with equivalent or inequivalent nearest neighbor hopping interactions, a feature of special interest is magnetic frustration. Thus, long-range magnetic ordering is increasingly frustrated if the lattice becomes more isotropic.

In Ref. [43] a cluster extension of DMFT combined with finite-temperature ED was used to study the Mott transition in two-dimensional frustrated systems, in particular, the variation of the T/U phase diagram with the degree of anisotropy. In the isotropic, fully frustrated limit ($t' = t$), the phase diagram is qualitatively similar to the one obtained within the single-site DMFT. On the other hand, for intermediate anisotropy $t' \approx 0.8t$, re-entrant behavior was found. Analogous QMC CDMFT results [88] also exhibit re-entrant behavior, albeit at higher temperatures. Also, only the phase boundary $U_{1c}(T)$ was determined. More recent continuous-time QMC DMFT calculations for $t' = 0.44t$ yield $T_c = 0.13t$ [89], in approximate agreement with the ED result, $T_c \approx 0.11t$ [43].

The unit cells employed in Ref. [43] consist of three sites, and the bath was assumed to contain six levels ($n_s = 9$). In Ref. [40] it was shown that, despite this small bath size, for $T = 0.02$ a rather accurate discretization of the bath Green's function is achieved ($t = 1$, band width $W = 9$). Figure 19 illustrates how the quality of this discretization improves further if three bath levels

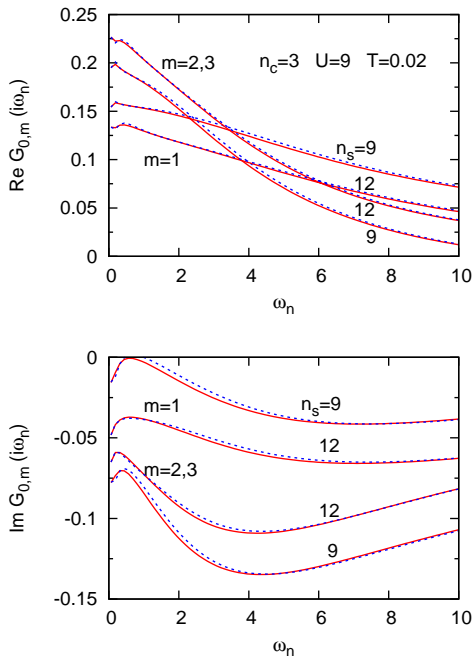


FIG. 19: (Color online) Discretization of bath Green's function components $G_{m,0}(i\omega_n)$ for isotropic triangular lattice using two ($n_s = 9$) and three ($n_s = 12$) bath levels per molecular orbital; $t = 1$, $U = 9$, $T = 0.02$. For clarity, the results for $n_s = 9$ are shifted up ($m = 1$) or down ($m = 2, 3$) by 0.025. Upper panel: real part; lower panel: imaginary part.

per site are included ($n_s = 12$). We consider here only the isotropic case $t' = t$, so that in the molecular-orbital basis the Green's function is diagonal, as indicated in Eq. (15). The components $G_{0,m}(i\omega_n)$ can then be discretized independently. Although the fit for $n_s = 9$ is already quite good, several more detailed low-energy features are reproduced better for $n_s = 12$.

Figure 20 shows the self-energy components for both bath sizes. The differences in this case are caused by the fact that the Coulomb energy $U = 9$ is very close to the lower boundary U_{c1} of the coexistence region [43]. Moreover, the value of U_{c1} is slightly smaller for $n_s = 9$ than for $n_s = 12$. Similar differences close to a phase boundary were also found in the degenerate three-band model discussed in Section 3.1, for instance, in the upper panel of Figure 4. The chemical potential $\mu = 3$ nearly coincides with the spin freezing transition, so that small changes due to different bath sizes can lead to larger changes in scattering rates and other dynamical properties. Thus, near phase boundaries the size of the bath plays a more subtle role. The important point, however, is that this merely affects the precise values of certain quantities, such as the critical Coulomb energies, and not the qualitative aspects of the phase diagram.

ED DMFT cluster spectra for isotropic and anisotropic triangular lattices can be found in Refs. [40] and [43],

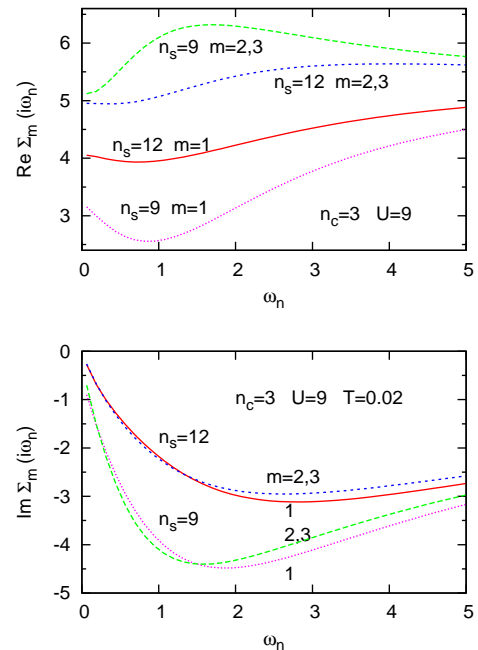


FIG. 20: (Color online) Self-energy components for isotropic triangular lattice using two ($n_s = 9$) and three ($n_s = 12$) bath levels per molecular orbital; $t = 1$, $U = 9$, $T = 0.02$. Upper panel: real part; lower panel: imaginary part.

respectively.

3.5. Square Lattice

One of the most widely studied applications of cluster DMFT is the two-dimensional Hubbard model for the square lattice which is believed to capture some of the essential ingredients of the physics of cuprate high-temperature superconductors. The parent compounds at half-filling are Mott insulators while in the overdoped region at large electron or hole concentrations ordinary Fermi-liquid behavior is observed. In the underdoped region, significant deviations from Fermi-liquid properties are found, including pseudogap formation and a strongly momentum dependent scattering rate along the Fermi surface. Evidently, such effects cannot be described within a single-site or local version of DMFT. The most natural unit cell for taking into account short-range fluctuations are 2×2 clusters as shown in the center diagram of Figure 2. Several groups have applied $T = 0$ ED CDMFT to investigate the non-local properties of the single-band Hubbard model for a square lattice [26–31].

Here we focus on the Hamiltonian defined in Eq. (13), with $t = 0.25$ and $t' = -0.075$ as first and second neighbor hopping interactions, respectively (band width $W = 2$). In Ref. [41] we have used finite-temperature

ED CDMFT to study various aspects of this model, in particular, the collective mode in the $(\pi, 0)$ component of the self-energy which gives rise to the opening of the pseudogap at low doping, the increase of the scattering rate with decreasing doping, and the striking asymmetry between electron and hole doping caused by the second-neighbor hopping t' . For instance, at $U = 10t = 2.5$ the Mott transition driven by electron doping is first-order, with characteristic hysteresis behavior of the orbital occupancies and double occupancy. In contrast, the transition induced by hole doping is continuous. In the latter case, upon doping the van Hove singularity at $(\pi, 0)$ shifts toward the Fermi energy, whereas for electron doping it moves away from E_F .

To implement ED CDMFT for the square lattice, we use the diagonal molecular-orbital or plaquette [27, 91] basis, as indicated in Eq. (16), which yields three independent Green's function and self-energy components ($m = 1, \dots, 3$). We denote them as $\Gamma = (0, 0)$, $M = (\pi, \pi)$, and $X = (\pi, 0)$, where the latter is degenerate with $Y = (0, \pi)$. Each of the impurity levels hybridizes only with its own bath consisting of two levels, as indicated in the left-hand diagram of Figure 1. The upper panels of Figure 21 show the discretization of the bath Green's function components via the supercluster consisting of impurity cluster plus bath. The Coulomb energy $U = 2.5$ is chosen so that at half-filling the system is a Mott insulator, where $U_c \approx 5.6t = 1.4$ [90]. The chemical potential $\mu = 0.5$ corresponds to about 8 % hole doping. At $T = 0.01$, each component $G_{0,m}(i\omega_n)$ is seen to be fitted very well with only five parameters: the impurity level, two bath levels, and two hopping terms. For completeness, the values are provided in Table I.

The results shown in Figure 21 are derived via minimization of $|G_0 - G_0^{cl}|$ as in Eq. (22), for $W_n = 1/\omega_n^N$ with $N = 1$. Appendix A.2 demonstrates that discretizations of similar accuracy are achieved for $N = 0$ and $N = 2$. Also, minimization of $|1/G_0 - 1/G_0^{cl}|$, as in Eq. (23), for $W_n = 1/\omega_n^N$, $N = 0, 1, 2$, is of nearly the same quality.

Transforming the molecular-orbital parameters back to the non-diagonal site basis, the values given in Table I yield the onsite level $\varepsilon = (\varepsilon_1 + \varepsilon_2 + 2\varepsilon_3)/4 = 0.0078$, and the hopping energies $\tau = -(\varepsilon_1 - \varepsilon_2)/4 = 0.2545 \approx t$, and $\tau' = -(\varepsilon_1 + \varepsilon_2 - 2\varepsilon_3)/4 = -0.078 \approx t'$. Thus, the impu-

TABLE I: Impurity levels ε_m , bath levels ε_k , and impurity bath hopping matrix elements $V_{m,k}$ for square lattice; $n_s = 12$, $U = 2.5$, $T = 0.01$, $\mu = 0.5$. The corresponding Green's function components are shown in Figure 21.

m	ε_m	$\varepsilon_{k=m+4}$	$\varepsilon_{k'=m+8}$	$V_{k=m+4}$	$V_{k'=m+8}$
1	-0.42339	0.03516	-0.05844	0.07602	0.09822
2	0.59461	-0.02611	0.10462	0.08436	0.17005
3	-0.07018	0.08829	-0.03705	0.13478	0.09028

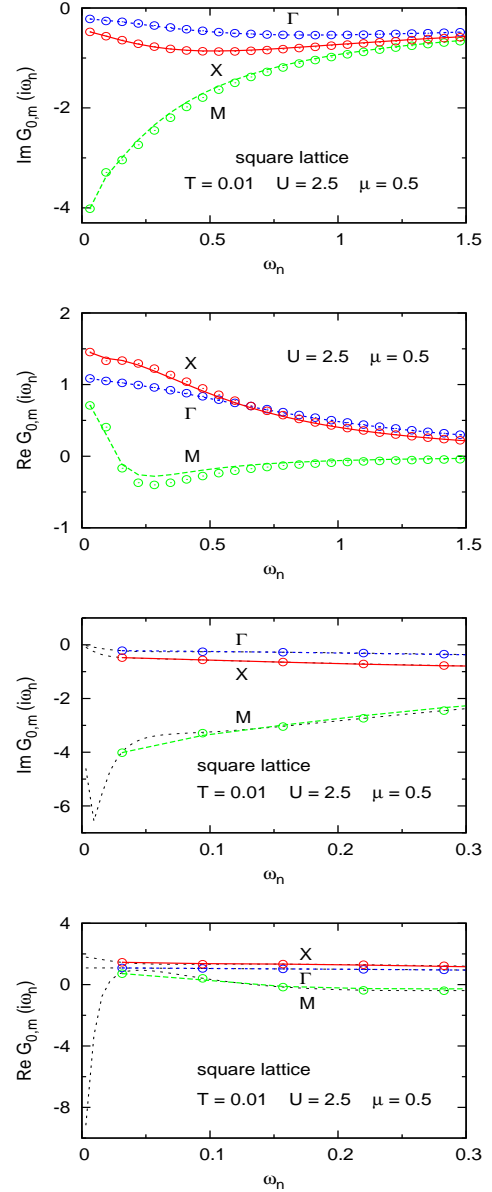


FIG. 21: (Color online) Upper two panels: Comparison of diagonal components of lattice bath Green's function $G_{0,m}(i\omega_n)$ (solid and dashed colored curves) and cluster Green's function $G_{0,m}^{cl}(i\omega_n)$ (symbols) for square lattice, using two bath levels per impurity molecular orbital ($n_s = 12$); $U = 2.5$, $T = 0.01$, $\mu = 0.5$ [41]. Lower two panels: Amplified low-energy region. Black dotted curves: $G_{0,m}^{cl}(i\omega_n)$ on a Matsubara grid corresponding to $T = 0.001$.

urity levels in the diagonal molecular-orbital basis are well determined by the asymptotic behavior of $G_0(i\omega_n)$. The small deviations from $\varepsilon = 0$, $\tau = t$, and $\tau' = t'$ suggest that at low ω_n a slightly more accurate discretization of G_0 can be achieved than by enforcing these conditions.

The two lower panels of Figure 21 show the low-energy region of $G_0(i\omega_n)$ in more detail. The dotted

black curves represent the cluster Green's function components $G_{0,m}^{cl}(i\omega_n)$ on a much finer Matsubara grid, corresponding to $T = 0.001$. Since cluster spectra are always gapped, large oscillations occur at low frequencies $\omega_n < 0.01\pi$, in order to accommodate the limit $\text{Im } G_{0,m}^{cl}(i\omega_n) \rightarrow 0$ for $\omega_n \rightarrow 0$. Evidently, more bath levels would be required to achieve a satisfactory representation of extremely low temperature and low frequency properties. [For the hopping $t = 1/4$ used here, the temperature in Fig. 14 of Ref. [30] is $T = t/256 = 1/1024$.] On the other hand, as long as the discussion is limited to temperatures of about $T = 0.005$ or higher, and to frequencies larger than about $\omega_0 = \pi T$, two bath levels per impurity orbital are adequate.

As shown in Ref. [41], temperatures in the range $T = 0.005, \dots, 0.010$ are low enough to provide evidence of a collective mode in the $(\pi, 0)$ component of the self-energy, once it is extrapolated from the Matsubara axis to real ω . This is illustrated in the upper panel of Figure 22, which reveals a transition from Fermi liquid properties in the overdoped region ($\delta > 15\%$) to pronounced non-Fermi-liquid behavior in the underdoped region ($\delta < 15\%$). These self-energies are derived via analytic continuation from the Matsubara axis to $\omega + i\gamma$ with $\gamma = 0.005$. The collective mode in $\text{Im } \Sigma_{(\pi,0)}(\omega)$ gives rise to strong damping of electronic states near E_F , consistent with a pseudogap in the quasi-particle density of states [28, 91]. This is also shown in Figure 22, where the middle panel represents cluster spectra at hole dopings $\delta = 0.03$ and $\delta = 0.18$ (broadening $\gamma = 0.02$), while the lower panel shows the corresponding spectra obtained via analytic continuation of the lattice Green's function to real ω . About 400...600 Matsubara points are taken into account and the same broadening is assumed as in the cluster spectra. The low-frequency behavior of both spectral distributions, in particular, the pseudogap slightly above E_F and the concomitant particle-hole asymmetry in the underdoped region, is seen to be in good agreement. Farther below or above E_F , the lattice and cluster spectra exhibit large differences. The lattice spectra can also be calculated by first extrapolating the self-energy to real frequencies and then evaluating Eq. (18) at real ω . The results are fully consistent with the spectra derived via direct extrapolation of the lattice Green's function.

Additional cluster spectra as a function of hole doping can be found in Ref. [92], which discusses the correlation-induced transfer of spectral weight between low and high energies in the two-dimensional Hubbard model.

A dynamical cluster calculation (DCA) for the square lattice was recently carried out for 4×4 clusters, using Hirsch-Fye QMC as an impurity solver [93]. Figure 23 shows the comparison of the $(\pi, 0)$ component of the self-energy at the lowest Matsubara frequency with the corresponding ED CDMFT results obtained in Ref. [41] for 2×2 clusters. Both approaches are in good agreement for doping $\delta \geq 0.1$. The difference at $\delta = 0.05$ is most likely

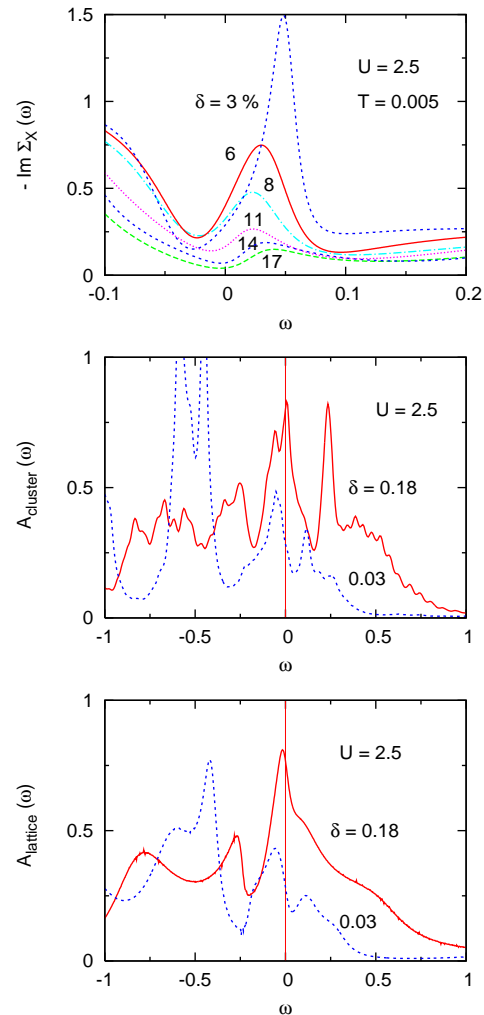


FIG. 22: (Color online) Upper panel: Low-energy region of imaginary part of self-energy $\Sigma_{X=(\pi,0)}(\omega)$ obtained via extrapolation to real frequencies for several hole doping concentrations (broadening $\gamma = 0.005$); $U = 2.5$, $T = 0.005$. Middle panel: Cluster spectral distributions. Solid red curve: hole doping $\delta = 0.18$ with peak at $E_F = 0$; dashed blue curve: $\delta = 0.03$ exhibiting a pseudogap above E_F . Lower panel: analogous spectra obtained via analytic continuation of lattice Green's function [41].

related to the singular nature of $\text{Im } \Sigma_{(\pi,0)}(i\omega_n)$ close to the Mott transition. Of course, the larger 4×4 cluster provides a much better momentum resolution, in particular, a better distinction between scattering properties along the nodal and anti-nodal directions of the Brillouin Zone. Nonetheless, the crossover from Fermi-liquid to non-Fermi-liquid behavior is driven by $\Sigma_{(\pi,0)}$ which is seen to be well represented within finite- T ED CDMFT. For a systematic study of the variation of the self-energy components with cluster size, see Ref. [94]. As also shown in Ref. [41], at lower temperature the Fermi-liquid to non-Fermi-liquid transition as a function of doping becomes

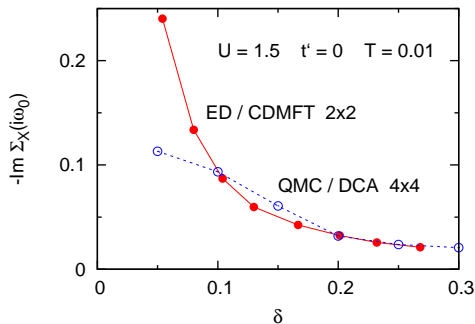


FIG. 23: (Color online) Imaginary part of self-energy component $\Sigma_{X=(\pi,0)}(i\omega_0)$ at first Matsubara frequency as a function of doping for $U = 1.5$, $t' = 0$, $T = 0.01$. Solid (red) symbols: ED CDMFT ($n_s = 12$) results for 2×2 clusters at $T = 0.01$ [41]; open (blue) symbols: QMC DCA results for 4×4 clusters at $T = 0.014$ [93].

sharper, in agreement with the QMC results in [93, 94].

The doping variation of the self-energy shown in Figure 23, with Fermi-liquid behavior in the overdoped region ($\delta > 0.2$), non-Fermi-liquid properties at lower doping ($0.05 < \delta < 0.15$), and a Mott phase at half-filling ($\delta = 0$), is strikingly similar to the one discussed above for the degenerate three-band and five-band models in sections 3.1 and 3.3, respectively. In the latter cases, Mott insulating phases may occur also at integer occupancies away from half-filling, but these tend to have considerably larger critical Coulomb energies [34, 47, 80]. On the other hand, at not too large values of U , these systems exhibit non-Fermi-liquid properties due to the formation of local moments, including a finite low-energy scattering rate, up to about one electron or hole away from half-filling, i.e., $|\delta| < 0.2, \dots, 0.3$. Only at larger doping, ordinary Fermi-liquid behavior is restored. Since multi-site correlations in the single-band Hubbard model may be formulated within a diagonal molecular-orbital basis, where the on-site repulsion is converted into intra-orbital and inter-orbital Coulomb and exchange interactions, the fact that common physical phenomena appear in both types of systems is plausible. The parallel treatment of these materials within DMFT, and the close relation between key physical properties, suggests that the existence of inter-orbital or inter-site interaction channels gives rise to fundamentally new physics that is absent in the single-band, single-site limit.

3.6. Honeycomb Lattice

We have recently used finite-temperature ED in combination with CDMFT to study the semi-metal to insulator transition in the honeycomb lattice at half-filling [42]. The Hubbard Hamiltonian is given by Eq. (13), with hop-

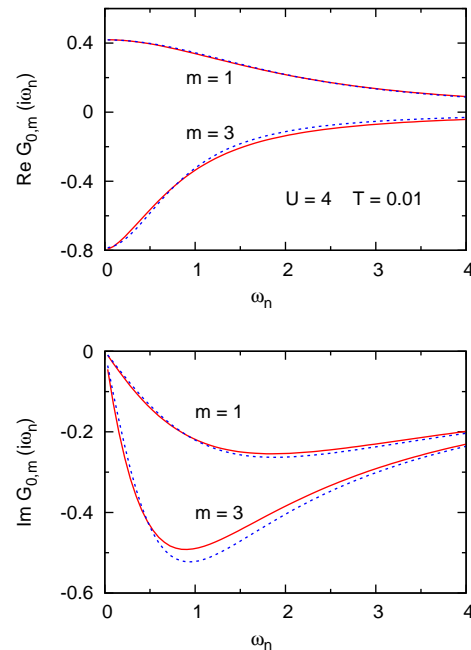


FIG. 24: (Color online) Comparison of lattice bath Green's function $G_{0,m}(i\omega_n)$ (solid red curves) and cluster Green's function $G_{0,m}^{cl}(i\omega_n)$ (dashed blue curves) for honeycomb lattice using only one bath level per impurity orbital ($n_s = 12$); $U = 4$, $T = 0.01$. Upper panel: real part; lower panel: imaginary part.

ping matrix elements $t_{ij} = t = 1$ for nearest neighbors and $t_{ij} = 0$ otherwise. The impurity cluster in which spatial fluctuations are accounted for explicitly consists of six sites, as illustrated in the right-hand diagram of Figure 2. Because of the symmetry of this cluster, the lattice Green's function can be diagonalized as indicated in Eq. (17). In the site basis G_{11} and $G_{13} = G_{15}$ are imaginary, while $G_{12} = G_{16}$ and G_{14} are real. Thus, the diagonal components satisfy $G_2 = -G_1^*$ and $G_4 = -G_3^*$, giving two independent complex functions. Analogous relations hold for the diagonal components of the cluster Green's function and self-energy. Although a $T = 0$ cluster calculation with two bath levels per impurity molecular orbital ($n_s = 18$) is feasible [95], the aim of this section is to demonstrate that, for the honeycomb lattice at half-filling, adequate results can be obtained even if only one bath level per impurity orbital is employed. Since for $n_s = 12$ the Hilbert space is still fairly large, the level spacing of interacting states is rather dense so that a reasonable representation of the low-energy behavior of the self-energy can be achieved.

As discussed in Section 2.4, one criterion for the accuracy of ED DMFT is the discretization of the lattice Green's function G_0 via the finite bath. In the present case, the k -sum on the right-hand side of Eq. (6) consists of only one term, so that each diagonal element

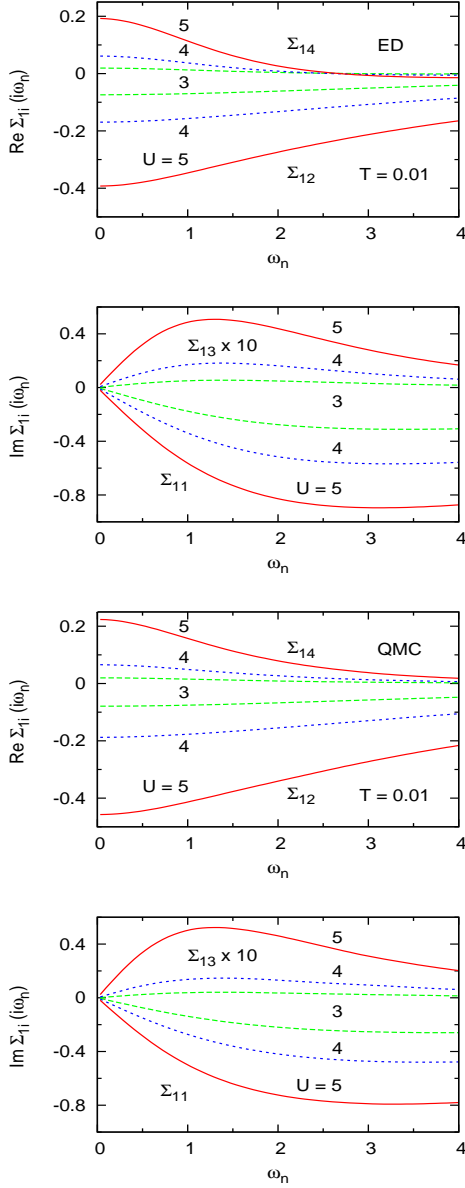


FIG. 25: (Color online) Self-energy components $\Sigma_{1i}(i\omega_n)$ ($i = 1, \dots, 4$) of honeycomb lattice obtained within cluster DMFT for three Coulomb energies at $T = 0.01$. For symmetry reasons, Σ_{11} and Σ_{13} are imaginary, while Σ_{12} and Σ_{14} are real. Upper two panels: ED [42]; lower two panels: continuous-time QMC [96].

$G_{0,m}(i\omega_n)$ is fitted with three parameters, the impurity level ε_m , the bath level ε_k , and the hopping term V_k , where $k = m + 6$. Figure 24 shows the comparison of the lattice and cluster Green's functions for $U = 4$, i.e., close to the Mott transition near $U_c \approx 3.5$. Comparisons of similar quality are found at $U = 3$ and $U = 5$, i.e., on the semi-metallic and insulating sides of the transition. Undoubtedly, one reason for the surprisingly good agreement is the semi-metallic nature at half-filling, which en-

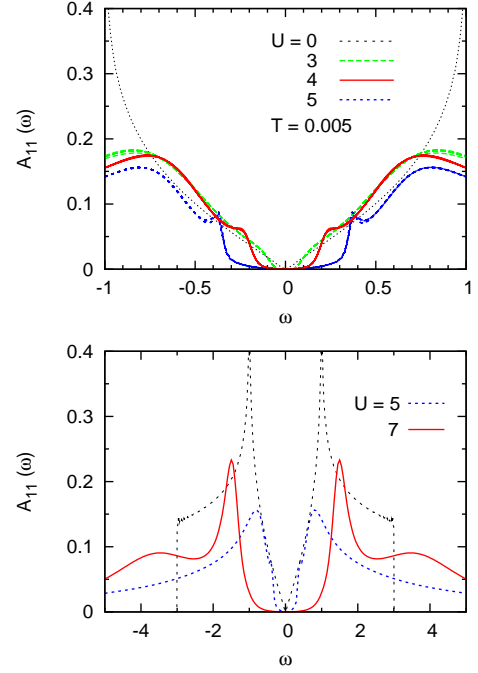


FIG. 26: (Color online) Upper panel: low-energy region of quasiparticle distribution of honeycomb lattice for several Coulomb energies at $T = 0.005$ [42]. The noninteracting density of states is indicated by the black dotted curve. Between 50 and 200 Matsubara points are used to extrapolate the lattice Green's function to real ω . Lower panel: density of states over wider energy range for $U = 5$ and $U = 7$.

sures that the imaginary part of the lattice Green's function vanishes in the limit of small ω_n even for $U < U_c$. Thus, there is no disparity here of representing a metallic lattice Green's function via a finite-size cluster Green's function.

The role of Coulomb correlations in the honeycomb lattice has recently also been studied within CDMFT by Wu *et al.* [96] who used continuous-time QMC as impurity solver. Figure 25 shows the ED and QMC self-energy components in the site basis, where Σ_{11} and Σ_{13} are imaginary, while Σ_{12} and Σ_{14} are real. The comparison at three different Coulomb energies ranging from the semi-metallic to the Mott insulating phases indicates that there is very good agreement between the ED and continuous-time QMC results. As can be seen in Refs. [42] and [96], similar agreement is found for the double occupancies and for the quasi-particle spectra.

Figure 26 (upper panel) shows the low-energy region of the interacting density of states for several Coulomb energies. These spectra are derived from an extrapolation of the local lattice Green's function $G_{11}(i\omega_n)$ to real ω . To illustrate the stability of this extrapolation, at each value of U several curves are plotted for 50 to 200 Matsubara points, with an additional small energy broadening of the order of $0.1\omega^2$. (For $|\omega| > 1$ the broad-

ening is kept constant at 0.1.) At $U = 3$, a tiny gap or pseudogap is seen which is near the limit of what can be resolved within ED/DMFT. At $U = 4$, a full gap of width $\Delta \approx 0.25$ has opened. Its width increases approximately to $\Delta \approx 0.6$ when the Coulomb energy is increased to $U = 5$. This trend is consistent with the one found in Refs. [96, 97]. The variation of the gap at larger U , and the appearance of Hubbard bands, are indicated in Figure 26 (lower panel). These results suggest that non-local correlations in the honeycomb lattice induce a paramagnetic semi-metal to insulator Mott transition in the range $U = 3 \dots 4$, in striking contrast to single-site DMFT which yields $U_c \approx 10 \dots 13$ [98, 99].

4. SUMMARY AND OUTLOOK

The accuracy of DMFT based on finite-temperature exact diagonalization has been discussed for a variety of strongly correlated materials. The cases include three-band and five-band single-site applications of DMFT, appropriate to transition metal compounds such as Ca_2RuO_4 , V_2O_3 , LaTiO_4 , Na_xCoO_2 , FeAsLaO , etc. In addition, short-range correlations in two-dimensional single-band Hubbard models are discussed for triangular, square, and honeycomb lattices, which represent key aspects of organic molecular crystals, high- T_c cuprates, and graphene. The main focus of this work is on the role of the temperature and size of the bath which is used to discretize the host lattice surrounding the correlated impurity. In contrast to the simpler single-band, single-site model, which requires typically 3 to 5 bath levels to achieve convergence, the multi-band and multi-site materials discussed here are usually well represented using two bath levels per orbital or site, as long as the temperature is not too low.

The accuracy of the results is illustrated using three different criteria: (i) the convergence of the self-energy with bath size, (ii) the quality of the discretization of the bath Green's function in terms of a finite cluster, and (iii) the comparison with analogous results obtained within continuous-time QMC DMFT. For a total of 10 to 15 impurity and bath levels, the Hilbert space for correlated multi-band or multi-site systems is rather large. Thus, because of the indirect coupling among the baths pertaining to different impurity levels, the spectrum of excited states is very dense, even if only two bath levels per impurity orbital or site are included. Moreover, at temperatures larger than 5 to 10 meV, the bath discretization is usually very accurate. At lower temperature, accordingly more bath levels per orbital or site should be employed. For five correlated orbitals within local DMFT only one bath level per orbital was found to give qualitatively correct results, including the transition from a Mott phase at half-filling to non-Fermi-liquid and Fermi-liquid behavior for increasing doping. Also, results

for the self-energy of the single-band Hubbard model on the honeycomb lattice at half-filling with only one bath level per site were found to be in excellent agreement with analogous QMC CDMFT results.

Since ED DMFT calculations, like those within QMC DMFT, are performed along the Matsubara axis, an extra step is needed to evaluate the Green's function and self-energy to real energies. An attractive feature of ED is that the cluster quantities can be calculated directly close to the real axis. Moreover, the corresponding lattice quantities can be derived via analytic continuation. As we have shown for several systems, this extrapolation is usually rather stable in the low-energy region, where the results agree well with the (broadened) cluster spectra.

The examples discussed in this paper suggest that finite-temperature ED DMFT is a versatile and accurate scheme for the description of electronic properties of a wide range of strongly correlated materials. It is applicable at large Coulomb energies and for full Hund exchange. Moreover, it is free of sign problems and statistical errors. Since it is most suitable at low temperatures ED DMFT can be regarded as complementary to continuous-time QMC DMFT. Studies at higher temperatures pose no problem in principle, but computational times increase due to the larger number of excited states that come into play. In the future it would be interesting to explore the correspondence between ED and QMC at higher temperatures than the ones discussed in the present work, and to establish the range of accuracy of both schemes at very low temperatures. It would also be very interesting to study more d -electron and possibly f -electron materials in order to investigate further the accuracy of ED DMFT when only one bath level per impurity orbital is included.

Acknowledgments. We like to thank M. Aichhorn, E. Gull, E. Koch, J. Merino, G. Sangiovanni, and Ph. Werner for useful discussions. Comments on the manuscript by E. Gull, D. Sénéchal, and A.-M. S. Tremblay are gratefully acknowledged. We also thank Philipp Werner for the QMC data in Figure 3 and Wei Wu for those in Figure 25. The numerical work was mainly carried out on the Juropa Computer of the Research Center Jülich.

a.liebsch@fz-juelich.de, ishida@chs.nihon-u.ac.jp

Appendix: Bath Discretization

One of the key approximations in ED DMFT is the discretization of the bath Green's function G_0 in terms of a finite cluster. Whereas G_0 for the infinite lattice is continuous at real ω , the analogous cluster version G_0^{cl} consists of a small number of discrete lines. Nonetheless, at finite temperatures both quantities are smooth functions along the imaginary Matsubara axis. To find

the bath levels ε_k and impurity–bath hopping matrix elements V_{mk} , the distance functions in Eq. (22) or (23) are minimized. Evidently, this minimization implies some uncertainty due to the different weight functions W_n that may be used to place more or less weight on the important low-energy region. In this Appendix we discuss in more detail the discretization of the bath Green’s function in the case of the three-band model (see Section 3.1) and the square lattice (Section 3.5).

A.1. Degenerate Three-Band Model

To illustrate the quality of the bath discretization more systematically, we show in Figure 27 the fits obtained for the three-band model discussed in Section 3.1 for weight functions $W_n = 1/\omega_n^N$ with $N = 0, 1, 2$. In all cases, the impurity levels are held fixed at $\varepsilon_{m=1,2,3} = 0$, in order to focus on the variation of the bath levels. Thus, there are four fit parameters per impurity orbital. The two upper panels are for the distance function specified in Eq. (22), while the lower panels are for minimization according to Eq. (23). The range of chemical potentials is chosen to cover the Fermi-liquid region ($\mu = 2$, $n \approx 1.5$) as well as the non-Fermi-liquid region close to the Mott phase ($\mu = 4$, $n \approx 2.5$). The intermediate case ($\mu = 3$, $n \approx 2$) is near the spin-freezing transition.

Figure 27 demonstrates that all six minimization procedures yield fits of good quality, in particular, for $N = 1$ and $N = 2$. Naturally, these fits imply slightly different bath parameters ε_k and V_{mk} . As shown in Figure 28, the differences between $N = 1$ and $N = 2$ are less pronounced than between $N = 1$ and $N = 0$. Also, fitting G_0 yields more stable ε_k and V_{mk} than fitting $1/G_0$. Since the bath parameters have only an auxiliary function, their variation does not have any physical significance. Their sole mathematical purpose is to provide an accurate representation of the frequency dependence of the lattice bath Green’s functions $G_{0,m}(i\omega_n)$, Eq. (4). Figure 28 indicates that smaller values of ε_k are associated with smaller values of V_{mk} . Because of this compensation, the quality of the various fits in Figure 27 is approximately the same.

The fits shown in Figure 27 are for a fixed set of lattice bath Green’s functions. We have also carried out complete self-consistency cycles using the six minimization procedures specified above. The resulting self-energies are in very good agreement. We therefore conclude that the arbitrariness caused by the discretization of the bath Green’s function is of minor importance in ED DMFT. On the whole, iteration to self-consistency is found to be most reliable and efficient for the distance function in Eq. (22), with $W_n = 1/\omega_n$.

A.2. Square Lattice

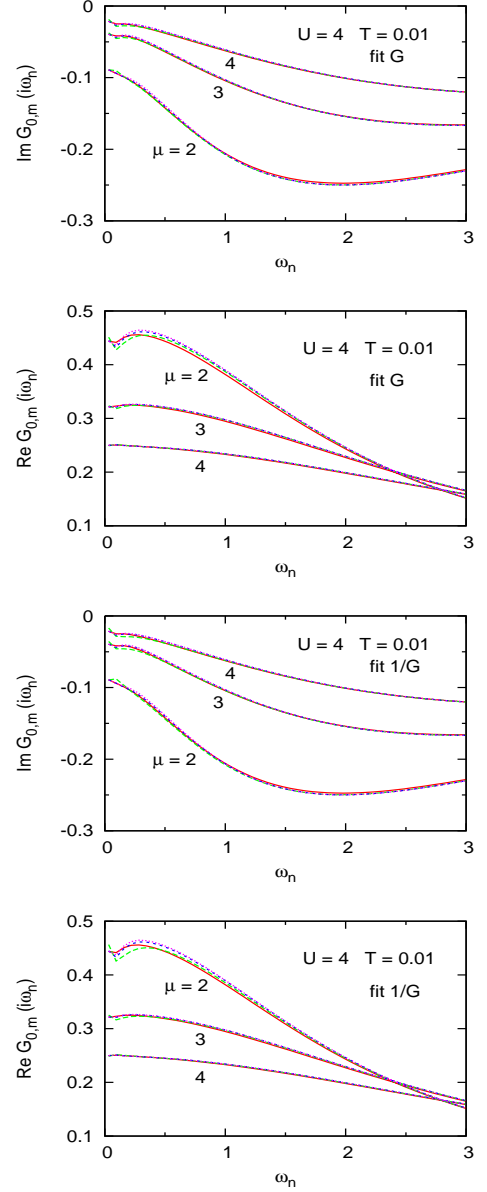


FIG. 27: (Color online) Discretization of bath Green’s function for degenerate three-band model as in Section 3.1 using two bath levels per impurity orbital ($n_s = 9$). Upper two panels: minimization of $|G_0 - G_0^{cl}|$, see Eq. (22); lower two panels: minimization of $|1/G_0 - 1/G_0^{cl}|$, see Eq. (23). Solid red curves: lattice bath Green’s function $G_{0,m}(i\omega_n)$ (same as in Figure 5); remaining curves: cluster Green’s functions derived for weight functions $W_n = 1/\omega_n^N$ with $N = 0$ (dashed green curves), $N = 1$ (dashed blue curves), and $N = 2$ (dotted magenta curves).

In Figure 21, we have illustrated the quality of the discretization of the bath Green’s function of the 2×2 square lattice for the three independent molecular orbitals corresponding to Γ , M , and X . The minimization was performed using Eq. (22) with the weight function $W_n = 1/\omega_n$. Figure 29 shows results of analogous dis-

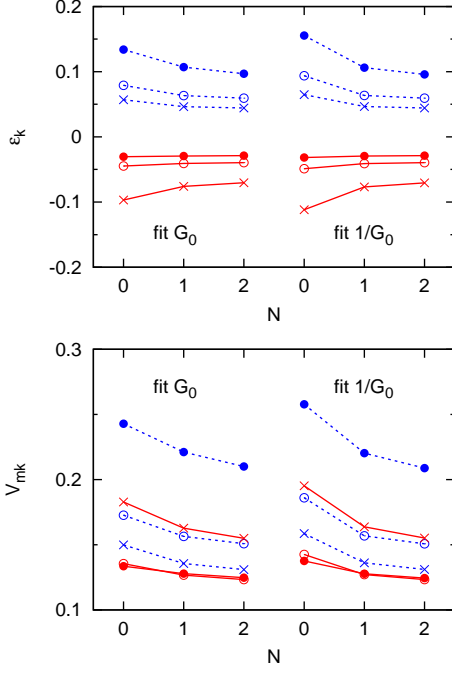


FIG. 28: (Color online) Bath levels ε_k (top panel) and hybridization matrix elements V_{mk} (lower panel) for fits in Figure 27. Solid dots: $\mu = 2$, empty dots: $\mu = 3$, x symbols: $\mu = 4$. Left: minimization of $|G_0 - G_0^{cl}|$, see Eq. (22); right: minimization of $|1/G_0 - 1/G_0^{cl}|$, see Eq. (23). The two bath levels are denoted by the red and blue colors.

cretizations using Eq. (22) as well as Eq. (23), for weight functions $W_n = 1/\omega_n^N$ with $N = 0, 1, 2$. The impurity levels ε_m are kept fixed at the values determined by the asymptotic behavior of $G_{0,m}$, as indicated in Eq. (19). Thus, there are four fit parameters per molecular orbital component $G_{0,m}$.

As in Figure 27, there is little difference among the six minimizations. Those for $N = 1$ and $N = 2$ are slightly more accurate than for $N = 0$. Figure 30 shows the variation of the bath levels ε_k and hopping matrix elements V_{mk} . Although there is considerable variation, in particular between $N = 1$ and $N = 0$, the net effect on the quality of the fit of $G_{0,m}$ using only two bath levels is small. Evidently, there is important compensation between the magnitudes of ε_k and V_{mk} . As in Figure 28, the differences between the results for $N = 1$ and $N = 2$ are much smaller than for $N = 1$ and $N = 0$. Also, fitting G_0 gives much more stable bath parameters than fitting $1/G_0$.

In Figs. 27 and 29 the bath and cluster Green's functions are compared since these are the important quantities used as input in the exact diagonalization. If the lattice and cluster hybridization functions [see Eqs. (24) and (25)] are compared instead, the differences at large ω_n are slightly larger since, in contrast to G_0 , these functions do not have unit asymptotic weight.

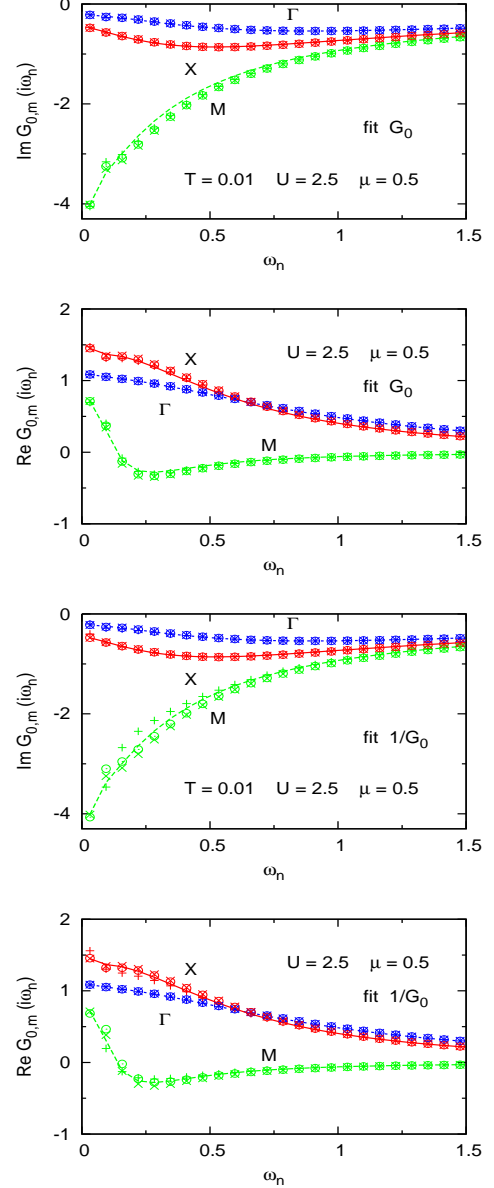


FIG. 29: (Color online) Discretization of bath Green's function for 2×2 square lattice as in Section 3.5. Solid and dashed curves: lattice bath Green's function $G_{0,m}(i\omega_n)$ (as in Figure 21). Upper two panels: real and imaginary parts of cluster Green's function $G_{0,m}^{cl}(i\omega_n)$ obtained via minimization of $|G_0 - G_0^{cl}|$, see Eq. (22), using two bath levels ($n_s = 12$) and weight functions $W_n = 1/\omega_n^N$ with $N = 0$ (+), $N = 1$ (o), and $N = 2$ (x). Lower two panels: analogous fits via minimization of $|1/G_0 - 1/G_0^{cl}|$, see Eq. (23).

- [1] W. Metzner and D. Vollhardt, Phys. Rev. Lett. **62**, 324 (1989).
- [2] E. Müller-Hardtman, Z. Phys. **74**, 507 (1989).
- [3] A. Georges, G. Kotliar, Phys. Rev. B **45**, 6479 (1992).
- [4] M. Jarrell, Phys. Rev. Lett. **69**, 168 (1992).

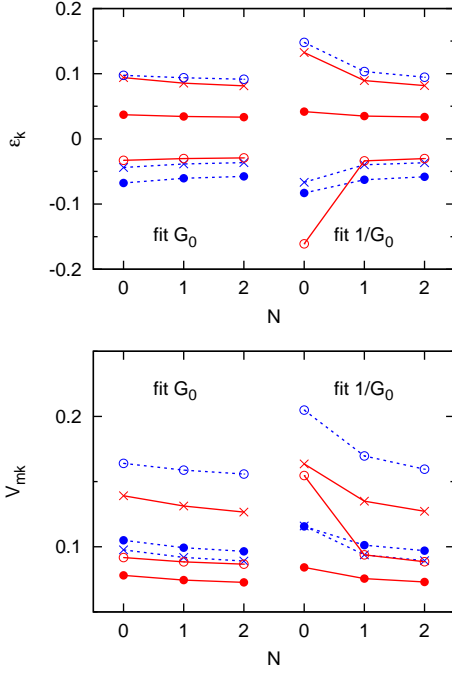


FIG. 30: (Color online) Bath levels ϵ_k (top panel) and hybridization matrix elements V_{mk} (lower panel) for fits in Figure 29. Solid dots: Γ , empty dots: M , x symbols: X . Left: minimization of $|G_0 - G_0^{cl}|$, see Eq. (22); right: minimization of $|1/G_0 - 1/G_0^{cl}|$, see Eq. (23). The two bath levels are denoted by the red and blue colors.

- [5] A. Georges, G. Kotliar, W. Krauth and M. J. Rozenberg, Rev. Mod. Phys. **68**, 13 (1996).
- [6] G. Kotliar and D. Vollhardt, Physics Today, March 53 (2004).
- [7] G. Kotliar, S. Y. Savrasov, K. Haule, V. S. Oudovenko, O. Parcollet, and C. A. Marianetti, Rev. Mod. Phys. **78**, 865 (2006).
- [8] K. Held, Adv. Phys. **56**, 829 (2007).
- [9] M. H. Hettler, A. N. Tahvildar-Zadeh, M. Jarrell, T. Pruschke, and H. R. Krishnamurthy, Phys. Rev. B **58**, R7475 (1998).
- [10] A. I. Lichtenstein and M. I. Katsnelson, Phys. Rev. B **62**, 9283(R) (2000).
- [11] G. Kotliar, S. Y. Savrasov, G. Palsson, and G. Biroli, Phys. Rev. Lett. **87**, 186401 (2001).
- [12] Th. A. Maier, M. Jarrell, T. Pruschke, and M. H. Hettler, Rev. Mod. Phys. **77**, 1027 (2005).
- [13] K. G. Wilson, Rev. Mod. Phys. **85**, 1508 (1975). H. R. Krishna-murthy, J. W. Wilkins, and K. G. Wilson, Phys. Rev. B **21**, 103 (1980).
- [14] R. Bulla, Th. A. Costi, and Th. Pruschke, Rev. Mod. Phys. **80**, 395 (2008).
- [15] J. E. Hirsch and R. M. Fye, Phys. Rev. Lett. **56**, 2521 (1986).
- [16] M. Caffarel and W. Krauth, Phys. Rev. Lett. **72**, 1545 (1994).
- [17] J. Jaklic and P. Prelovcek, Phys. Rev. B **49**, 5065 (1994); Adv. Phys. **49**, 1 (2000).
- [18] M. Aichhorn, M. Daghofer, H. G. Evertz, and W. von der Linden, Phys. Rev. B **67**, 195105 (2003).
- [19] A. Liebsch, Phys. Rev. Lett. **95**, 116402 (2005).
- [20] C. A. Perroni, H. Ishida, and A. Liebsch, Phys. Rev. B **75**, 045125 (2007).
- [21] M. Capone, L. de' Medici, and A. Georges, Phys. Rev. B **76**, 245116 (2007).
- [22] A. N. Rubtsov, V. V. Sarkin, and A. I. Lichtenstein, Phys. Rev. B **72**, 035122 (2005).
- [23] Ph. Werner, A. Comanac, L. de' Medici, M. Troyer, and A. J. Millis, Phys. Rev. Lett. **97**, 076405 (2006).
- [24] E. Gull, A. J. Millis, A. I. Lichtenstein, A. N. Rubtsov, M. Troyer, and Ph. Werner, Rev. Mod. Phys. **83**, 349 (2011).
- [25] C. J. Bolech, S. S. Kancharla, and G. Kotliar, Phys. Rev. B **67**, 075110 (2003).
- [26] M. Capone, M. Civelli, S. S. Kancharla, C. Castellani, and G. Kotliar, Phys. Rev. B **69**, 195105 (2004).
- [27] M. Civelli, M. Capone, S. S. Kancharla, O. Parcollet, and G. Kotliar, Phys. Rev. Lett. **95**, 106402 (2005).
- [28] B. Kyung, S. S. Kancharla, D. Sénéchal, A.-M. S. Tremblay, M. Civelli, and G. Kotliar, Phys. Rev. B **73**, 165114 (2006).
- [29] J. Merino, Phys. Rev. Lett. **99**, 036404 (2007).
- [30] E. Koch, G. Sangiovanni, and O. Gunnarsson, Phys. Rev. B **78**, 115102 (2008).
- [31] S. Sakai, Y. Motome, and M. Imada, Phys. Rev. Lett. **102**, 056404 (2009).
- [32] D. Sénéchal, Phys. Rev. B **81**, 235125 (2010).
- [33] R. B. Lehoucq, D. C. Sorensen, and C. Yang, ARPACK *Users' Guide* (SIAM, Philadelphia, 1997).
- [34] H. Ishida and A. Liebsch, Phys. Rev. B **81**, 054513 (2010).
- [35] M. Jarrell and J. E. Gubernatis, Phys. Rep. **269**, 133 (1969).
- [36] M. Potthoff and W. Nolting, Phys. Rev. B **59**, 2549 (1999); *ibid.* **60**, 7834 (1999).
- [37] H. Ishida and A. Liebsch, Phys. Rev. B **82**, 045107 (2010); *ibid.* **79**, 045130 (2009).
- [38] S. Sugano, Y. Tanabe, H. Kamimura, *Multiplets of transition-metal ions in crystals* (Academic press, New York and London), 1970.
- [39] For a derivation of this result within the so-called cavity method, see Ref. [5], Eq. (35), and: A. I. Lichtenstein and M. I. Katsnelson, Phys. Rev. B **57**, 6884 (1998).
- [40] A. Liebsch, H. Ishida, and J. Merino, Phys. Rev. B **78**, 165123 (2008).
- [41] A. Liebsch and N.-H. Tong, Phys. Rev. B **80**, 165126 (2010).
- [42] A. Liebsch, Phys. Rev. B **83**, 035113 (2011).
- [43] A. Liebsch, H. Ishida, and J. Merino, Phys. Rev. B **79**, 195108 (2009).
- [44] H. Ishida and A. Liebsch, Phys. Rev. B **82**, 045107 (2010).
- [45] X. Wang, E. Gull, L. de' Medici, M. Capone, and A. J. Millis, Phys. Rev. B **80**, 045101 (2009).
- [46] W. H. Press, S. A. Teukolsky, W. T. Vetterling, and B. P. Flannery, *Numerical Recipes in Fortran 77*, Cambridge University Press, p. 106 (1986-1992).
- [47] P. Werner, E. Gull, M. Troyer, and A. J. Millis, Phys. Rev. Lett. **101**, 166405 (2008).
- [48] P. Werner, E. Gull, and A. J. Millis, Phys. Rev. B **79**, 115119 (2009).
- [49] L. de' Medici, Phys. Rev. B **83**, 205112 (2011); L. de' Medici, J. Mravlje, and A. Georges, arXiv:1106.0815.

- [50] C. Raas, P. Grete, and G. S. Uhrig, *Phys. Rev. Lett.* **102**, 076406 (2009).
- [51] A. P. Mackenzie and Y. Maeno, *Rev. Mod. Phys.* **75**, 657 (2003).
- [52] T. Oguchi, *Phys. Rev. B* **51**, 1385 (1995); D. J. Singh, *Phys. Rev. B* **52**, 1358 (1995).
- [53] A. Liebsch and A. Lichtenstein, *Phys. Rev. Lett.* **84**, 1591 (2000).
- [54] V. I. Anisimov, I. A. Nekrasov, D. E. Kondakov, T. M. Rice, and M. Sigrist, *Eur. Phys. J. B* **25**, 191 (2002).
- [55] Z. V. Pchelkina, I. A. Nekrasov, Th. Pruschke, A. Sekiyama, S. Suga, V. I. Anisimov, and D. Vollhardt, *Phys. Rev. B* **75**, 035122 (2007).
- [56] A. Liebsch and H. Ishida, *Phys. Rev. Lett.* **98**, 216403 (2007).
- [57] L. Mravlje, M. Aichhorn, T. Miyake, K. Haule, G. Kotliar, and A. Georges, *Phys. Rev. Lett.* **106**, 096401 (2011).
- [58] L. Mravlje, private communication.
- [59] Z. Fang, N. Nagaosa, and K. Terakura, *Phys. Rev. B* **69**, 045116 (2004); Z. Fang and K. Terakura, *Phys. Rev. B* **64**, 020509(R) (2001).
- [60] E. Gorelov, M. Karolak, T. O. Wehling, F. Lechermann, A. I. Lichtenstein, and E. Pavarini, *Phys. Rev. Lett.* **104**, 226401 (2010).
- [61] L. de' Medici, S. R. Hassan, M. Capone, and Xi Dai, *Phys. Rev. Lett.* **102**, 126401 (2009).
- [62] E. Pavarini, S. Biermann, A. Poteryaev, A. I. Lichtenstein, A. Georges, and O. K. Andersen, *Phys. Rev. Lett.* **92**, 176403 (2004).
- [63] H. Ishida and A. Liebsch, *Phys. Rev. B* **77**, 115350 (2008).
- [64] F. J. Wong, S.-H. Baek, R. V. Chopdekar, V. V. Mehta, H.-W. Jang, Ch.-B. Eom, and Y. Suzuki, *Phys. Rev. B* **81**, 161101(R) (2010).
- [65] A. Othomo, D. A. Mueller, J. L. Grazul, and H. Y. Hwang, *Nature (London)* **419**, 378 (2002).
- [66] A. Liebsch, *Phys. Rev. B* **77**, 115115 (2008).
- [67] G. Keller, K. Held, V. Eyert, D. Vollhardt, and V. Anisimov, *Phys. Rev. B* **70**, 205116 (2004).
- [68] T. Pruschke and R. Bulla, *Eur. Phys. J. B* **44**, 217 (2005).
- [69] K. Takada, H. Sakurai, E. Takayama-Muromachi, F. Izumi, R. A. Dilanian, and T. Sasali, *Nature (London)* **422**, 53 (2003);
- [70] D. J. Singh, *Phys. Rev. B* **61**, 13397 (2000).
- [71] M. Z. Hasan, Y.-D. Chuang, D. Qian, Y. W. Li, Y. Kong, A. Kuprin, A. V. Fedorov, R. Kimmerling, E. Rotenberg, K. Rosnagel, Z. Hussain, H. Koh, N. S. Rogado, M. L. Foo, and R. J. Cava, *Phys. Rev. Lett.* **92**, 246402 (2004).
- [72] H.-B. Yang, S.-C. Wang, A. K. P. Sekharan, H. Matsui, S. Souma, T. Sato, T. Takahashi, T. Takeuchi, J. C. Campuzano, R. Jin, B. C. Sales, D. Mandrus, Z. Wang, and H. Ding, *Phys. Rev. Lett.* **92**, 246403 (2004).
- [73] H. Ishida, M. D. Johannes, and A. Liebsch, *Phys. Rev. Lett.* **94**, 196401 (2005).
- [74] A. Liebsch and H. Ishida, *Eur. Phys. J. B* **61**, 405 (2008).
- [75] F. Lechermann, S. Biermann, and A. Georges, *Prog. Theor. Phys. Suppl.* **160**, 233 (2005).
- [76] C. A. Marianetti, K. Haule, and O. Parcollet, *Phys. Rev. Lett.* **99**, 246404 (2007).
- [77] C. A. Marianetti, private communication.
- [78] D. Pillay, M. D. Johannes, and I. I. Mazin, *Phys. Rev. Lett.* **101**, 246808 (2008).
- [79] T. Miyake, L. Poudrovskii, V. Vildosola, S. Bierman, and A. Georges, *J. Phys. Soc. Jpn.* **77** Suppl. C, 99 (2008).
- [80] A. Liebsch and H. Ishida, *Phys. Rev. B* **81**, 155105 (2010).
- [81] A. A. Katanin, A. I. Poteryaev, A. V. Efremov, A. O. Shorikov, S. L. Skornyakov, M. A. Korotin, and V. I. Anisimov, *Phys. Rev. B* **81**, 045117 (2010).
- [82] A. Liebsch, *Phys. Rev. B* **84**, xxx (2011).
- [83] Z. P. Yin, K. Haule, and G. Kotliar, *Nature Physics* **7**, 294 (2011).
- [84] N. L. Wang, W. Z. Hu, Z. G. Chen, R. H. Yuan, G. Li, G. F. Chen, and T. Xiang, arXiv:1105.3939.
- [85] A. A. Schafgans, S. J. Moon, B. C. Pursley, A. D. LaForge, M. M. Qazilbash, A. S. Sefat, D. Mandrus, K. Haule, G. Kotliar, and D. N. Basov, arXiv:1106.3114.
- [86] S. Lefebvre, P. Wzietek, S. Brown, C. Bourbonnais, D. Jérôme, C. Mézière, M. Fourmigué, and P. Batail, *Phys. Rev. Lett.* **85**, 5420 (2000).
- [87] Y. Kurosaki, Y. Shimizu, K. Miyagawa, K. Kanoda, and G. Saito, *Phys. Rev. Lett.* **95**, 177001 (2005).
- [88] T. Ohashi, T. Momoi, H. Tsunetsugu, and N. Kawakami, *Phys. Rev. Lett.* **100**, 076402 (2008).
- [89] M. Sentef, Ph. Werner, E. Gull, and A. P. Kampf, *Phys. Rev. B* **84**, 165133 (2011).
- [90] H. Park, K. Haule, and G. Kotliar, *Phys. Rev. Lett.* **101**, 186403 (2008).
- [91] M. Jarrell, Th. Maier, M. H. Hettler, and A. N. Tahvildarzadeh, *Europhys. Lett.* **56**, 563 (2001).
- [92] A. Liebsch, *Phys. Rev. B* **81**, 235133 (2010).
- [93] N. S. Vidhyadhiraja, A. Macridin, C. Sen, M. Jarrell, and M. Ma, *Phys. Rev. Lett.* **102**, 206407 (2009).
- [94] E. Gull, M. Ferrero, O. Parcollet, A. Georges, and A. J. Millis, *Phys. Rev. B* **82**, 155101 (2010).
- [95] L. Cano-Corts, J. Merino, and S. Fratini, *Phys. Rev. Lett.* **105**, 036405 (2010).
- [96] W. Wu, Y.-H. Chen, H.-Sh. Tao, N.-H. Tong, and W.-M. Liu, *Phys. Rev. B* **82**, 245102 (2010), and: W. Wu, private communication.
- [97] Z. Y. Meng, T. C. Lang, S. Wessel, F. F. Assaad, and A. Muramatsu, *Nature* **464**, 847 (2010).
- [98] S. A. Jafari, *Eur. Phys. J. B* **68**, 537 (2009).
- [99] M. T. Tran and K. Kuroki, *Phys. Rev. B* **79**, 125125 (2009).